

# Controlled Tension Forecasting: Quantifying Cross-Probe Biases in $\omega_0\omega_a$ CDM

Seokcheon Lee<sup>1</sup>

<sup>1</sup>*Department of Physics, Institute of Basic Science, Sungkyunkwan University, Suwon 16419, Korea*  
(Dated: December 5, 2025)

Recent analyses combining DESI DR2 BAO, Planck CMB, and Pantheon+ SNe have reported mild but intriguing deviations from the  $\Lambda$ CDM model. A central challenge is to determine whether these deviations reflect genuine dynamical dark energy behavior or instead arise from cross-probe inconsistencies, prior choices, or mismatches in likelihood construction. Previous work demonstrated that imposing a biased supernova-motivated prior on  $\Omega_{m0}$  can artificially displace the BAO-inferred  $(\omega_0, \omega_a)$  values from the  $\Lambda$ CDM expectation. A complementary pedagogic study further showed that the differing degeneracy geometries of BAO, CMB, and SNe can generate apparent dark energy evolution even when the underlying cosmology is exactly  $\Lambda$ CDM. In this manuscript, we develop a controlled tension injection framework that provides a systematic means of quantifying how probe-level tensions influence inferred dark energy parameters. Self-consistent BAO, CMB, and SNe mock datasets are augmented with parameterized shifts in  $(\Omega_{m0}, H_0)$ , supernova absolute calibration, and the BAO sound-horizon scale  $r_d$ . The resulting datasets are analyzed through a unified MCMC pipeline, enabling a direct assessment of how these controlled tensions propagate into biases in  $(\omega_0, \omega_a)$  and the pivot equation-of-state parameter  $\omega_p$ . This forecasting framework provides practical guidance for identifying probe combinations that are most susceptible to spurious signatures of dynamical dark energy, and helps ensure robust multi-probe inference in forthcoming precision surveys.

## CONTENTS

I. Introduction	2
II. Methodology	4
A. Connection to <i>Paper1</i>	4
B. Pedagogic CPL Null Test as a Baseline	4
C. Mock Generation	4
D. BAO, CMB, and SNe Likelihood Structure	5
E. Methodological Pipeline and Modular Structure	5
III. Forecasting Framework	5
A. Tension Parameters	6
B. Controlled Tension Injection Scheme	6
1. Data-level injections	6
2. Prior-level injections	7
3. Hybrid injections	7
C. MCMC Pipeline for Tension Forecasts	7
1. Likelihood construction	7
2. Parameter vector and priors	7
3. Joint sampling	7
4. Fisher-based bias estimates	7
IV. Results from the Controlled Tension-Injection Runs	8
A. Run1: Tension-Free Baseline Joint Analysis	8
B. Run2: SNe $H_0$ ( $+3\sigma$ ) Tension via Zero-Point Shift	8
1. Posterior Shifts and Degeneracy Geometry	9
2. Tension-Injection Mechanism	10
3. Pivot Equation-of-State	10
4. Joint Posterior Contours	10
C. Run3: BAO $\Omega_{m0}$ Tension via Distance-Ratio Distortion	10
1. Posterior Shifts and Degeneracy Geometry	11
2. Tension-Injection Mechanism	12
3. Pivot Equation-of-State	12

4. Joint Posterior Contours	12
D. Run4: CMB Acoustic-Scale Tension via Low- $H_0$ Distance Prior	13
1. Posterior Shifts and Degeneracy Geometry	14
2. Tension-Injection Mechanism	14
3. Pivot Equation-of-State	15
4. Joint Posterior Contours	15
E. Run5: Opposite-Directed BAO–CMB Tensions	15
1. Posterior Shifts and Degeneracy Geometry	15
2. Tension-Injection Mechanism	15
3. Pivot Equation-of-State	17
4. Joint Posterior Contours	17
F. Run6: SNe Anchor Miscalibration (Zero-Point Shift)	17
1. Posterior Shifts and Degeneracy Geometry	17
2. Tension-Injection Mechanism	18
3. Pivot Equation-of-State	19
4. Joint Posterior Contours	19
G. Run7: Combined Multi-Probe Systematic Tension	19
1. Posterior Shifts and Degeneracy Geometry	19
2. Tension-Injection Mechanism	20
3. Pivot Equation-of-State	21
4. Joint Posterior Contours	21
V. Empirical tension–bias transfer functions	21
A. One-Dimensional Tension–Bias Relations	21
1. Tension in $\Omega_{m0}$	22
2. Tension in $H_0$	22
3. SNe absolute-magnitude tension	23
B. From One-Dimensional Fits to a Multi-Dimensional Tension–Bias Map	23
1. Construction of the Bias Matrix	23
2. Two-Dimensional Bias Maps and Vector Diagrams	23
3. Predicting Multi-Probe Biases	24
C. Limitations of the One-Dimensional Transfer Functions	24
VI. Discussion	26
VII. Conclusion	26
A. Technical Supplement: Controlled Tension Injection and Fisher-Level Bias Propagation	27
1. Science Rationale and Conceptual Goals	27
2. Design of the Controlled Tension Pipeline	27
3. Fisher-Level Bias from SNe Calibration Drift	27
4. Fisher-Level Bias from $\Delta\Omega_{m0}$ , $\Delta H_0$ , and $\Delta r_d$	28
5. Analytic Derivatives for DESI BAO and CMB Distance Priors	28
6. Forecasting Workflow	28
Acknowledgments	29
References	29

## I. INTRODUCTION

The question of whether dark energy (DE) deviates from a cosmological constant remains central to modern cosmology. Recent analyses of DESI DR2 baryon acoustic oscillations (BAO) [1–3], Pantheon+ supernovae (SNe) [4–9], and cosmic microwave background (CMB) compressed distance priors [10–14] have reported mild indications that  $\omega_0\omega_a$ CDM provides a slightly more flexible phenomenological description than  $\Lambda$ CDM when heterogeneous probes are combined [15–26]. Some prominent BAO and SNe studies have even claimed robust evidence for dynamical dark energy (DDE) [27–29]. However, these deviations typically have low statistical significance and are highly sensitive

to prior choices, assumptions regarding the sound-horizon scale  $r_d$ , and the internal consistency of the individual probes [30–32].

A substantial body of work has emphasized that cross-probe tensions—including the well-known  $H_0$  discrepancy between CMB and distance-ladder measurements, as well as inconsistencies between BAO and SNe—or hidden systematics can mimic DDE signatures [33–38]. Notably, DES supernova analyses have shown that low-redshift calibration systematics or anchor choices can bias  $\Omega_{m0}$  and induce apparent DDE-like behavior [39] when analyzed using the Chevallier–Polarski–Linder (CPL) parametrization [40, 41]. This issue has been sharpened by studies demonstrating that the DESI DR1/DR2 claims for evolving DE may be significantly biased by low-redshift SNe systematics [42]. A recent Bayesian analysis further found that much of the reported preference for  $\omega_0\omega_a$ CDM arises not from true sensitivity to DE evolution, but from the ability of  $(\omega_0, \omega_a)$  to absorb the  $\sim 3\sigma$  tension between DESI DR2 BAO and DES-Y5 SNe within the  $\Lambda$ CDM framework [28].

A complementary pedagogic CPL null test [43] reinforced this point by constructing fully self-consistent DESI-like BAO, Planck-like CMB, and Pantheon+-like SNe mocks from a single fiducial  $\Lambda$ CDM cosmology. Even in the complete absence of injected tensions, these probes exhibit distinct degeneracy geometries in the  $(\omega_0, \omega_a)$  plane [44, 45]. When analyzed individually, the probe-dependent ridge structures can induce mild shifts that visually resemble DDE-like trends while remaining fully compatible with the underlying  $\Lambda$ CDM cosmology, similar to patterns observed in real data. Only the full BAO+CMB+SNe combination correctly recovers the fiducial parameters, demonstrating the necessity of multi-probe coherence for robust DE inference [46, 47].

These developments motivate a systematic method to understand how realistic cross-probe inconsistencies affect inferred DE properties. As increasingly precise observations introduce subtle calibration differences, low-redshift anchors, and  $r_d$  dependencies, the need for a transparent framework that quantifies how such mismatches influence  $(\omega_0, \omega_a, \omega_p)$  has become clear [38, 48–50]. In particular, recent assessments of observational constraints have emphasized that interpreting DDE requires extreme care [31, 32], while the broader theoretical context of CPL-based forecasting and the role of pivot formulations has been extensively studied since the DETF report [51], with further methodological refinements provided in Refs. [52–54].

Beyond these methodological considerations, the parametrization itself can introduce additional systematic structure. Several recent studies have highlighted intrinsic limitations of the CPL parametrization itself when applied to heterogeneous or partially inconsistent datasets. These include its strong sensitivity to basis choices, degeneracy-geometry distortions, and prior-induced artifacts [55–59]. Such works collectively emphasize that apparent deviations from  $\Lambda$ CDM inferred within the CPL framework may arise from structural features of the parametrization rather than from genuine time evolution of the DE equation of state (EoS).

The goal of this paper is to develop a general controlled tension-injection forecasting framework. We introduce parameterized inconsistencies in key quantities such as  $\Omega_{m0}$ ,  $H_0$ , the SNe absolute magnitude, redshift-dependent SNe tilts, and the BAO sound horizon  $r_d$ , while keeping all other aspects of the mocks construction internally consistent. These controlled mismatches are propagated through a unified MCMC engine applied to BAO, CMB, SNe, and all their combinations. By comparing the resulting posteriors to a tension-free baseline, we quantify how specific cross-probe inconsistencies manifest as apparent shifts in  $(\omega_0, \omega_a, \omega_p)$  and other cosmological parameters.

This framework bridges the prior-bias analysis of Ref. [38], the degeneracy-geometry null tests of Ref. [43], and the broader effort to understand cross-probe tensions in the era of DESI, Pantheon+, and Planck. It provides a transparent, modular, and systematic approach for interpreting next-generation multi-probe datasets with percent-level precision and for ensuring that apparent DDE signals are not artifacts of probe-level inconsistencies.

Finally, the remainder of this paper is organized as follows. In Sec. II, we describe the methodological foundations of our framework, including the construction of fully self-consistent  $\Lambda$ CDM mocks, the tension-free baseline analysis, and the unified Markov Chain Monte Carlo (MCMC) pipeline used for all probe combinations. Section III introduces the parameterized tension models, detailing the individual mismatch channels we consider—such as shifts in  $\Omega_{m0}$ ,  $H_0$ , the SNe absolute calibration, redshift-dependent SNe tilts, and the BAO sound-horizon scale  $r_d$ —along with the hybrid and probe-specific tension-injection schemes. In Sec. IV, we present the main results of the controlled tension-injection runs. We quantify how the injected mismatches propagate into apparent shifts in  $(\omega_0, \omega_a, \omega_p)$  across BAO-only, CMB-only, SNe-only, and all joint-probe configurations, thereby identifying which channels and probe pairings are most susceptible to spurious indications of DDE. Section V provides a complementary, empirical characterization of these effects by constructing tension–bias transfer functions that map specific injected inconsistencies to the resulting posterior distortions. In Sec. VI, we discuss the methodological and observational implications of our findings for next-generation surveys, with particular emphasis on diagnosing cross-probe inconsistencies and informing optimal multi-probe analysis strategies for DESI, Pantheon+, Rubin/Legacy Survey of Space and Time (LSST) [60], and forthcoming CMB experiments such as LiteBIRD [61] and the Simons Observatory [62]. Finally, Section VII summarizes our conclusions and outlines directions for future applications, including survey-optimized tension modeling, pipeline stress testing, and integration with full-likelihood cosmological analyses.

## II. METHODOLOGY

In this section, we summarize the methodological backbone of our controlled tension-injection framework. We first review the key lessons from previous analysis (hereafter *Paper1*) and from the pedagogic CPL null-test project (hereafter *Paper2*), which jointly motivate the forecasting framework developed in this paper. In what follows, we focus on the conceptual and mathematical structure of the analysis, with implementation-level details kept implicit to highlight the essential methodology.

### A. Connection to *Paper1*

The starting point for the present forecasting framework is Ref. [38] (*Paper1*), which investigated how biased external priors on  $\Omega_{m0}$  can distort the DE constraints inferred from DESI DR2 BAO data. In that work, we considered a fiducial flat  $\Lambda$ CDM cosmology

$$(\Omega_{m0}^{\text{fid}}, H_0^{\text{fid}}, \omega_0^{\text{fid}}, \omega_a^{\text{fid}}) = (0.30, 70 \text{ kms}^{-1}\text{Mpc}^{-1}, -1, 0), \quad (1)$$

and analyzed DESI-like BAO distance-ratio observables ( $D_M(z)/r_d$  and  $D_H(z)/r_d$ ) using the full tracer-resolved covariance matrix from DESI DR2 [2]. The central methodological element of *Paper1* was to impose a Gaussian prior on  $\Omega_{m0}$ ,

$$\pi(\Omega_{m0}) \propto \exp \left[ -\frac{(\Omega_{m0} - \Omega_{m0}^{\text{prior}})^2}{2\sigma_{\Omega_m}^2} \right], \quad (2)$$

with  $\Omega_{m0}^{\text{prior}}$  motivated by a Pantheon+-like SNe analysis and deliberately displaced relative to the adopted fiducial value  $\Omega_{m0}^{\text{fid}} = 0.30$ . This setup allowed us to quantify how a mismatched SNe-based prior on  $\Omega_{m0}$  biases the BAO-inferred CPL parameters, even when the underlying cosmology is exactly  $\Lambda$ CDM.

Three methodological lessons from *Paper1* directly motivate the present work. First, the BAO likelihood alone defines a well-behaved degeneracy ridge in  $(\omega_0, \omega_a)$  whose location is highly sensitive to assumptions about  $\Omega_{m0}$ . Second, even a moderate prior offset  $\Delta\Omega_{m0} \equiv \Omega_{m0}^{\text{prior}} - \Omega_{m0}^{\text{fid}}$  can generate  $\mathcal{O}(0.1)$  shifts in  $(\omega_0, \omega_a)$  that visually mimic the patterns often interpreted as mild DDE signatures. Third, such shifts arise from the partial-likelihood structure—BAO combined with an external prior—rather than from genuine inconsistencies among independent datasets. The present forecasting framework generalizes this logic by introducing controlled cross-probe tensions across BAO, CMB, and SNe, thereby transforming a single prior-bias example into a systematic multi-probe assessment of parameter sensitivity.

### B. Pedagogic CPL Null Test as a Baseline

As a complementary foundation, *Paper2* [43] constructed fully self-consistent DESI-like BAO, Planck-like CMB distance-prior, and Pantheon+-like SNe mocks from a shared fiducial  $\Lambda$ CDM cosmology. In contrast to *Paper1*, no external priors were enforced, and no cross-probe tensions were introduced. The objective was to establish how much of the apparent DDE-like behaviour in real data could be reproduced solely from intrinsic likelihood geometry, from the differing degeneracy directions probed by each dataset, and from the complementarity of multi-probe combinations.

*Paper2* demonstrated that each probe individually occupies a distinct degeneracy direction in the  $(\Omega_{m0}, H_0, \omega_0, \omega_a)$  parameter space, producing mild but coherent shifts in  $(\omega_0, \omega_a)$  when analyzed separately. These shifts arise not from systematics or injected tensions, but from the fact that BAO, CMB, and SNe probe different redshift ranges and combinations of cosmological parameters. They are therefore geometric rather than physical in origin. When the three probes are combined coherently, the fiducial  $\Lambda$ CDM parameters are correctly recovered, establishing a natural tension-free baseline for the present framework. Any bias observed in later sections can thus be attributed unambiguously to the injected inconsistencies rather than hidden effects in the mock construction.

### C. Mock Generation

Throughout this work, we adopt the fiducial cosmology in Eq. (1) as the tension-free baseline and generate DESI-like BAO, Planck-like CMB, and Pantheon+-like SNe mock observables in a fully consistent manner. The emphasis is on reproducing the statistical properties and covariance structure of the surveys rather than software-specific implementation details. For the BAO sector, we compute the distance ratios  $D_M(z)/r_d$  and  $D_H(z)/r_d$  at the effective

redshifts of the DESI tracers, using covariance matrices matched to DESI DR2. For the CMB distance prior, we construct the compressed vector  $\{R, \ell_A, \omega_b\}$  with means and covariances calibrated to Planck-2018-like constraints, where  $R$  is the CMB shift parameter and  $\ell_A$  the acoustic angular scale. The SNe sector uses a Pantheon+-like Hubble-diagram dataset with full statistical and systematic covariance, with  $M$  marginalized as a standard nuisance parameter and optional redshift-dependent tilts  $\Delta M(z)$  included in tension-injection tests.

Mock data vectors are drawn from multivariate normal distributions,

$$\mathbf{d}_{\text{mock}} = \mathbf{d}_{\text{th}}(\theta_{\text{fid}}) + L \mathbf{g}, \quad (3)$$

where  $L$  is the Cholesky factor of the survey covariance and  $\mathbf{g}$  a vector of standard normal deviates [63–65]. This yields a self-consistent baseline dataset to which controlled tensions are later applied either by modifying selected components of the synthetic data or by altering the parameter assumptions entering the likelihood.

#### D. BAO, CMB, and SNe Likelihood Structure

All probes are analyzed in a unified CPL parameter space,

$$\theta = \underbrace{\{\Omega_{m0}, H_0, \omega_0, \omega_a, r_d\}}_{\text{cosmological}}, \underbrace{\{M, \Delta M(z)\}}_{\text{SNe nuisance}}, \underbrace{\{\delta_{\text{rd}}, \delta H_0, \delta \Omega_{m0}\}}_{\text{tension parameters}}, \quad (4)$$

where  $(\Omega_{m0}, H_0, \omega_0, \omega_a)$  are the primary cosmological parameters;  $r_d$  is the BAO sound horizon;  $M$  is the SNe absolute magnitude;  $\Delta M(z)$  denotes optional redshift-dependent SNe distortions; and  $(\delta_{\text{rd}}, \delta H_0, \delta \Omega_{m0})$  represent the controlled offset parameters that encode the injected cross-probe inconsistencies introduced in Sec. III. Only a subset of these parameters is active in any given analysis, with the remainder fixed or set to zero in the tension-free baseline.

Each likelihood is assumed Gaussian in the data vector,

$$-2 \ln \mathcal{L}_X(\theta) = [\mathbf{d}_X^{\text{obs}} - \mathbf{d}_X^{\text{th}}(\theta)]^T C_X^{-1} [\mathbf{d}_X^{\text{obs}} - \mathbf{d}_X^{\text{th}}(\theta)], \quad (5)$$

with BAO using  $\{D_M/r_d, D_H/r_d\}$ , CMB using  $\{R, \ell_A, \omega_b\}$ , and SNe using  $\mu(z)$  with optional  $\Delta M(z)$ . Joint analyses use the product likelihood under the assumption that probe-specific covariances adequately capture internal systematics. In our framework, the tension-injection parameters modify only the theoretical predictions, leaving the baseline mocks unchanged and ensuring that any shift in the recovered posteriors originates solely from the injected inconsistency.

#### E. Methodological Pipeline and Modular Structure

The full methodology is implemented using a modular analysis pipeline that cleanly separates cosmological calculations, mock generation, likelihood evaluation, and sampling. Cosmological distances, Hubble functions, and BAO ratios are computed within a common CPL module; mock datasets are generated using survey-covariance infrastructure; and BAO, CMB, and SNe likelihoods share a unified parameter interface. Sampling is performed using a coherent MCMC framework applied consistently across all probe combinations. This modular organization ensures that the tension-free baseline and the tension-injected analyses differ only through the controlled offsets applied to the theoretical predictions, enabling an unambiguous interpretation of the resulting parameter biases. No changes are made to the mock data vectors or covariances, ensuring a clean separation between statistical fluctuations and injected systematic mismatches.

### III. FORECASTING FRAMEWORK

This section introduces the core components of our controlled tension-injection forecasting methodology. We first define the tension parameters used to characterize probe-specific inconsistencies in cosmological inference. We then describe the controlled injection scheme by which these inconsistencies are implemented in otherwise self-consistent BAO, CMB, and SNe mock datasets. Finally, we present the unified MCMC and Fisher-analysis pipeline through which the injected tensions propagate into posterior distortions of  $(\omega_0, \omega_a, \omega_p)$  and related cosmological parameters.

## A. Tension Parameters

A key goal of this work is to treat cross-probe inconsistencies as explicit, controllable parameters. To this end, we introduce the tension vector

$$\Delta \mathbf{t} = \left( \Delta \Omega_{m0}, \Delta H_0, \Delta M, \Delta M(z), \Delta r_d, \Delta d_{\text{BAO}}(z), \Delta \mu(z) \right), \quad (6)$$

where each component represents a physically interpretable mismatch that can be selectively applied to BAO, CMB, or SNe predictions. Throughout this paper, the mock catalogs themselves are kept internally consistent; the tension parameters modify only the model predictions  $\mathbf{d}_X^{\text{th}}(\theta)$ .

The full tension vector includes matter-density-like offsets  $(\Delta \Omega_{m0}, \Delta H_0)$ , SNe calibration shifts  $(\Delta M, \Delta M(z))$ , BAO-scale distortions  $(\Delta r_d, \Delta d_{\text{BAO}}(z))$ , and optional SNe-distance perturbations  $\Delta \mu(z)$ . For clarity, the dominant components used in our controlled experiments are:

- $\Delta \Omega_{m0}$  (BAO–CMB–SNe matter-density tension),
- $\Delta H_0$  (CMB–SNe Hubble tension),
- $\Delta M$  (SNe zero-point calibration offset),
- $\Delta r_d$  (BAO sound-horizon offset).

For the concrete tension-injection experiments discussed in Sec. IV, we restrict attention to the reduced tension vector

$$\Delta \mathbf{t} = (\Delta \Omega_{m0}, \Delta H_0, \Delta M, \Delta r_d), \quad (7)$$

which captures the dominant mismatch channels driving cross-probe inconsistencies in DESI–Planck–Pantheon+. These four components are sufficient to reproduce the leading posterior shifts in  $(\omega_0, \omega_a, \omega_p)$ .

For clarity and reproducibility, we summarize the mapping between these tension components and the specific tension-injection runs (runs 2–7). These runs constitute the controlled experiments whose results are presented in Sec. IV.

- **run2:** SNe-driven  $H_0$  tension from a controlled zero-point shift ( $\Delta M \neq 0$ ).
- **run3:** BAO matter-density tension from  $\Delta \Omega_{m0} \neq 0$ .
- **run4:** CMB sound-horizon tension from  $\Delta r_d \neq 0$ .
- **run5:** BAO–CMB Opposite-sign tension (combined offsets in  $\Delta \Omega_{m0}$  and  $\Delta r_d$ ).
- **run6:** SNe anchor–miscalibration scenario with ( $\Delta M \neq 0$ ) inducing an effective  $\Delta H_0$ .
- **run7:** Combined multi-probe tension using simultaneous offsets in  $(\Delta \Omega_{m0}, \Delta H_0, \Delta M, \Delta r_d)$ .

This mapping provides a direct link between the theoretical structure of the tension vector and the practical tension scenarios implemented in our forecasts.

## B. Controlled Tension Injection Scheme

Given a specified tension vector  $\Delta \mathbf{t}$ , we introduce probe-specific inconsistencies in a controlled and traceable manner. Three injection modes are distinguished.

### 1. Data-level injections

The theoretical predictions entering the mock generation are modified prior to adding survey noise

$$\mathbf{d}_X^{\text{obs}} = \mathbf{d}_X^{\text{th}}(\theta_{\text{fid}}) + \Delta \mathbf{d}_X(\Delta \mathbf{t}) + L_X \mathbf{g}. \quad (8)$$

Examples include SNe zero-point shifts ( $M \rightarrow M + \Delta M$ ), BAO-scale distortions ( $r_d \rightarrow r_d + \Delta r_d$ ), or CMB distance-prior shifts modifying  $(R, \ell_A)$  to emulate an  $H_0$  mismatch. These represent miscalibrated data or probe-internal systematics.

## 2. Prior-level injections

The mock data remain tension-free, but the likelihood analysis uses a biased external prior, e.g.

$$\pi(\Omega_{m0}) = \mathcal{N}(\Omega_{m0}^{\text{fid}} + \Delta\Omega_{m0}, \sigma_{\Omega_m}^2). \quad (9)$$

This corresponds to the prior-bias mechanism identified in Paper 1.

## 3. Hybrid injections

Some realistic scenarios require combining data-level and prior-level offsets. Typical examples include a higher SNe-inferred  $H_0$  induced by  $\Delta M$  together with CMB priors preferring a lower  $H_0$ , or BAO distance calibrations shifted by  $\Delta r_d$  while CMB keeps the fiducial  $r_d$ . Hybrid schemes emulate multi-probe inconsistencies linked to distinct physical quantities.

## C. MCMC Pipeline for Tension Forecasts

Once a tension scenario is imposed, the resulting mock datasets are analyzed using the same unified MCMC pipeline as the tension-free baseline. This ensures that any differences in the recovered posteriors arise solely from the injected inconsistencies.

### 1. Likelihood construction

Each probe enters through the Gaussian likelihood

$$-2 \ln \mathcal{L}_X(\theta) = [\mathbf{d}_X^{\text{obs}} - \mathbf{d}_X^{\text{th}}(\theta)]^\top C_X^{-1} [\mathbf{d}_X^{\text{obs}} - \mathbf{d}_X^{\text{th}}(\theta)]. \quad (10)$$

### 2. Parameter vector and priors

The sampled cosmological parameter vector is  $\theta = (\Omega_{m0}, H_0, \omega_0, \omega_a, r_d, M)$ , with flat priors for baseline analyses and appropriately biased priors for prior-level tension injections.

### 3. Joint sampling

Probe combinations (BAO+CMB, BAO+SNe, BAO+CMB+SNe) are sampled by multiplying the individual likelihoods. We use `emcee` with 128 walkers, a 2000-step burn-in, and a 5000-step production run [66]. The MCMC output includes marginalized posteriors, median constraints, pivot parameters  $(a_p, z_p, w_p)$ , and derived summaries of posterior geometry.

### 4. Fisher-based bias estimates

To complement the MCMC forecasts, we compute the Fisher matrix

$$F_{\alpha\beta} = \left\langle \frac{\partial^2 \chi^2}{\partial \theta_\alpha \partial \theta_\beta} \right\rangle_{\text{fid}}, \quad (11)$$

and derive linear-response bias estimates

$$\Delta\theta_\alpha^{(\text{Fisher})} = \sum_\beta (F^{-1})_{\alpha\beta} \left( \frac{\partial \chi^2}{\partial \theta_\beta} \right)_{\Delta \mathbf{t}}. \quad (12)$$

Comparison with the full MCMC results quantifies the accuracy of the linear-response approximation and provides a functional tension–bias mapping for each injection scenario.

Together, the tension parameters, controlled injection scheme, and unified MCMC–Fisher pipeline form a coherent architecture for quantifying how cross-probe inconsistencies propagate into apparent shifts in DE parameters. This forecasting framework is transparent, reproducible, and readily extensible to next-generation datasets and alternative DE parametrizations.

#### IV. RESULTS FROM THE CONTROLLED TENSION-INJECTION RUNS

Before presenting the individual tension-injection experiments, we provide a brief overview of the structure of this section. Runs 2–7 constitute a suite of controlled tests in which specific components of the tension vector  $\Delta\mathbf{t}$  are selectively perturbed to emulate well-motivated cross-probe inconsistencies. Each run isolates a distinct mismatch channel (*e.g.*, SNe zero-point shifts, BAO matter-density offsets, or CMB sound-horizon perturbations), allowing us to quantify how these controlled deviations propagate into posterior distortions of  $(\omega_0, \omega_a, \omega_p)$  and related parameters. Run1 serves as the tension-free reference analysis against which all subsequent tension runs are evaluated. The following subsections present the results of run1–run7 in increasing order of complexity, highlighting the characteristic bias signatures associated with each injected inconsistency.

##### A. Run1: Tension-Free Baseline Joint Analysis

Run1 establishes the tension-free baseline against which all subsequent tension-injection experiments (run2–7) are evaluated. In this configuration, no artificial offsets are introduced into any of the probes, and the BAO, CMB, and SNe mock datasets are generated from the common fiducial flat  $\Lambda$ CDM cosmology. All tension parameters are set to zero,  $\Delta\Omega_{m0} = \Delta H_0 = \Delta M = \Delta r_d = 0$ , so that the three probes form a mutually consistent dataset with no internal inconsistencies.

The joint BAO+CMB+SNe analysis of this configuration provides an essential null test. The MCMC sampling yields the following median and  $1\sigma$  constraints:

$$\begin{aligned}\Omega_{m0} &= 0.2964 \pm 0.0033, & H_0 &= 69.861 \pm 0.229, \\ \omega_0 &= -1.0138 \pm 0.0416, & \omega_a &= 0.1440 \pm 0.1370.\end{aligned}\tag{13}$$

These posteriors lie within  $1\sigma$  of the fiducial values  $(0.30, 70, -1, 0)$ , and the  $(\omega_0, \omega_a)$  pair aligns with the standard CPL degeneracy band that passes through  $(-1, 0)$ . No systematic displacement is observed in any direction, indicating that the likelihood geometry and numerical integrations behave precisely as expected in the absence of tension.

The corresponding pivot EoS parameters are

$$a_p = 0.7177, \quad z_p = 0.3933, \quad \omega_p = -0.9738 \pm 0.0147,\tag{14}$$

again statistically consistent with the fiducial value  $\omega_p = -1$ . This confirms that the pipeline faithfully reconstructs  $\Lambda$ CDM when the input mocks contain no probe-level inconsistencies.

Run1 therefore provides the reference point for all subsequent tension runs. Because the baseline analysis recovers the fiducial cosmology without bias, any deviations observed in run2–run7 must be attributed to the intentionally injected probe-specific inconsistencies rather than numerical artifacts. Moreover, Run1 specifies the intrinsic width and orientation of the CPL degeneracy directions in the  $(\omega_0, \omega_a)$  plane, supplying the geometric framework against which tension-induced shifts can be systematically interpreted.

Figure 1 displays the joint posterior for  $(\Omega_{m0}, H_0, \omega_0, \omega_a)$ . The contours are centered on the fiducial point and trace the familiar CPL degeneracy direction, with no observable displacement or rotation. This confirms that Run1 serves as a high-fidelity benchmark against which all tension-injection experiments can be robustly evaluated.

##### B. Run2: SNe $H_0$ (+3 $\sigma$ ) Tension via Zero-Point Shift

Run2 introduces a controlled tension exclusively in the supernova sector, designed to emulate a SH0ES-like preference for a higher Hubble constant. This is implemented through a coherent negative shift in the SNe absolute magnitude,  $\Delta M = -0.09$ , corresponding to a  $+3\sigma$  increase in the SNe-inferred Hubble constant ( $H_0^{\text{SNe}} \simeq 73 \text{ km s}^{-1} \text{ Mpc}^{-1}$ ) [67]. The BAO and CMB mocks remain fiducial, ensuring that any observed inconsistency in the joint BAO+CMB+SNe posterior originates solely from the SNe calibration bias.



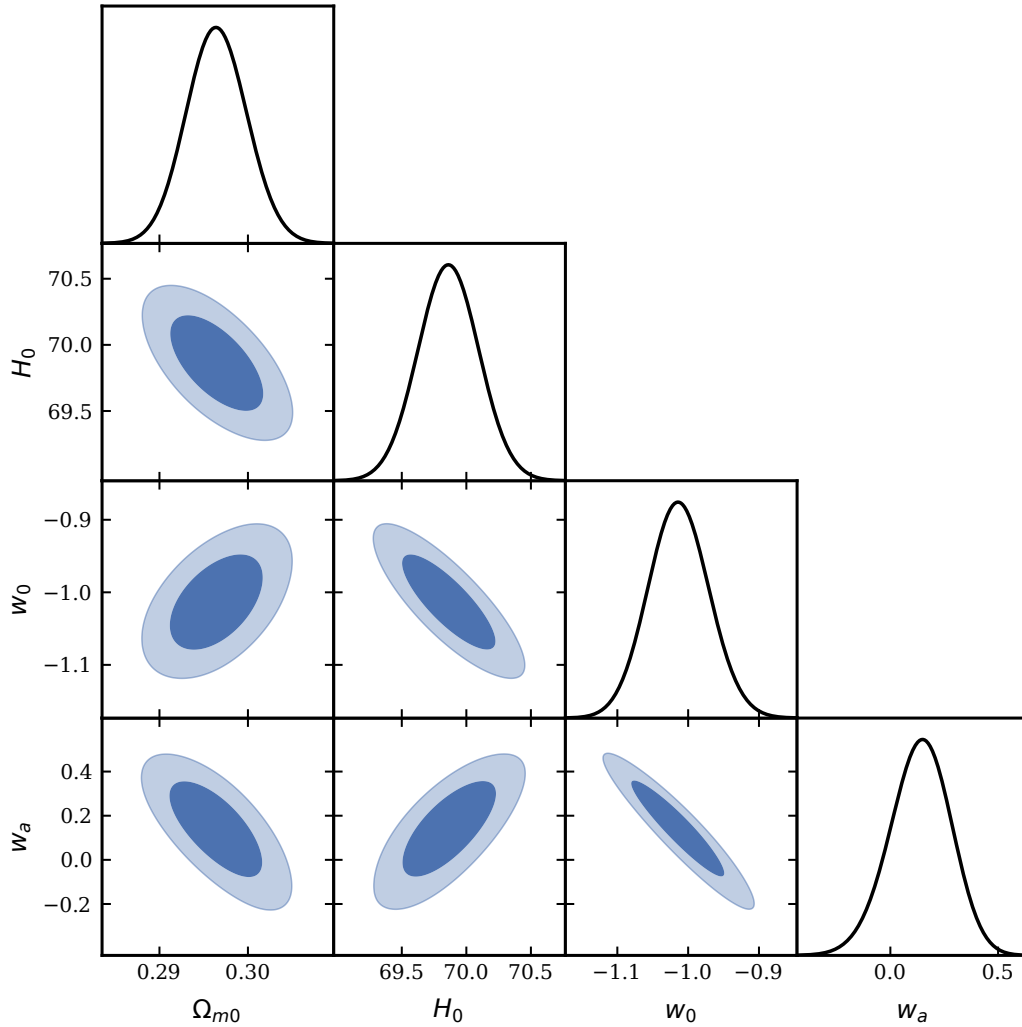


FIG. 1. **Run1 (tension-free baseline).** Joint posterior for BAO + CMB + SNe without any injected tension. The recovered parameters are fully consistent with the input  $\Lambda$ CDM cosmology, demonstrating the internal consistency of the mock datasets and validating the unified likelihood pipeline.

### 1. Posterior Shifts and Degeneracy Geometry

The joint MCMC constraints obtained in run2 are

$$\begin{aligned} \Omega_{m0} &= 0.3283 \pm 0.0036, & H_0 &= 66.362 \pm 0.210, \\ \omega_0 &= -0.9096 \pm 0.0392, & \omega_a &= 0.1507 \pm 0.1150. \end{aligned} \quad (15)$$

Compared with the fiducial cosmology, the joint posterior exhibits a coherent pattern of parameter shifts: the matter density is displaced to higher values, the inferred Hubble constant moves noticeably below the fiducial value, and the CPL parameters migrate toward the region  $(\omega_0 > -1, \omega_a > 0)$  typically associated with mild DDE.

At first sight these trends appear counterintuitive, since the SNe zero-point shift  $\Delta M < 0$  drives the SNe-only likelihood toward larger  $H_0$  and smaller  $\Omega_{m0}$ . However, the BAO and CMB likelihoods impose much stronger degeneracy constraints, and these dominate the geometry of the combined posterior. DESI-like BAO observables favor decreasing  $H_0$  in combination with increasing  $\Omega_{m0}$  in order to preserve the distance ratios  $D_M/r_d$  and  $D_H/r_d$ , while the CMB acoustic scale  $(R, \ell_A)$  remains most stable when a decrease in  $H_0$  is accompanied by a shift toward  $(\omega_0 > -1, \omega_a > 0)$ . Because BAO and CMB have significantly greater constraining power than SNe, the joint posterior is pulled along their shared degeneracy direction rather than along the SNe-preferred trend. This explains why the global fit moves toward  $(H_0 \downarrow, \Omega_{m0} \uparrow, \omega_0 > -1, \omega_a > 0)$  even though the injected SNe calibration bias alone would have favored the

opposite direction.

The qualitative degeneracy directions are summarized in Table I.

TABLE I. Qualitative degeneracy directions relevant for run2. Despite the SNe zero-point tension ( $\Delta M < 0$ ) pushing the SNe-only posterior toward higher  $H_0$ , the much tighter BAO and CMB constraints enforce the opposite trends in the joint analysis.

Probe	Dominant Degeneracy Direction	Physical Origin
SNe	$(H_0 \uparrow, \Omega_{m0} \downarrow)$	$\Delta M < 0$ increases inferred luminosity, raising $H_0$
BAO	$(H_0 \downarrow, \Omega_{m0} \uparrow)$	Preserve $D_M/r_d$ and $D_H/r_d$ ratios
CMB	$(H_0 \downarrow, \omega_0 > -1, \omega_a > 0)$	Maintain $(R, \ell_A)$ acoustic consistency

## 2. Tension-Injection Mechanism

The tension is injected by applying a uniform shift to the SNe distance modulus from  $\mu_{\text{th}}(z)$  to  $\mu_{\text{th}}(z) + \Delta M$  with  $\Delta M = -0.09$ . Since the distance module is given by

$$\mu = m - M = 5 \log_{10} \left( \frac{D_L}{\text{Mpc}} \right) + 25, \quad (16)$$

where a negative shift in  $M$  corresponds to a brighter absolute magnitude and thus a smaller inferred luminosity distance for a fixed observed magnitude  $m$ . This moves the SNe-only posterior toward a significantly higher Hubble constant. Crucially, the shift is coherent across all SNe, modifying only the global distance scale without affecting the observational covariance matrix. BAO and CMB mocks remain unchanged, ensuring that any subsequent inconsistency is a pure SNe-versus-(BAO+CMB) tension. The resulting cross-probe conflict forces the joint likelihood to follow the BAO+CMB ridge rather than the SNe-preferred direction, thereby producing the net shifts in Eq. (15).

## 3. Pivot Equation-of-State

The pivot EoS parameters for run2 are

$$a_p = 0.6850, \quad z_p = 0.4599, \quad \omega_p = -0.8626 \pm 0.0130. \quad (17)$$

The large deviation of  $\omega_p$  from  $-1$  demonstrates that a single-probe calibration bias—here confined entirely to the SNe distance scale—can induce an apparently significant ( $> 3\sigma$ ) departure from a cosmological constant. This highlights one of the core lessons of the controlled-tension analysis: posterior deviations from  $\Lambda$ CDM do not necessarily imply DDE, but may originate from cross-probe inconsistencies.

## 4. Joint Posterior Contours

Figure 2 shows the full joint posterior for  $(\Omega_{m0}, H_0, \omega_0, \omega_a)$  in run2. Relative to the tension-free baseline, the contours shift coherently along the combined BAO+CMB degeneracy direction. Although this displacement would normally be interpreted as evidence for DDE, in this case it arises solely from the imposed SNe zero-point miscalibration.

## C. Run3: BAO $\Omega_{m0}$ Tension via Distance-Ratio Distortion

In run3 we introduce a controlled tension localized in the BAO sector. This construction is motivated by recent discussions of mild but persistent BAO–CMB inconsistencies in the matter-density sector [36, 68], wherein BAO analyses tend to favour slightly lower values of  $\Omega_{m0}$  than those inferred from CMB. This construction mimics a situation in which DESI-like BAO analyses favour a value of  $\Omega_{m0}$  that is systematically lower than that preferred by the CMB and SNe, while keeping the CMB distance priors and SNe luminosity-distance data fully consistent with the fiducial cosmology. To achieve this, the BAO observables  $D_M/r_d$  and  $D_H/r_d$  are distorted along their intrinsic

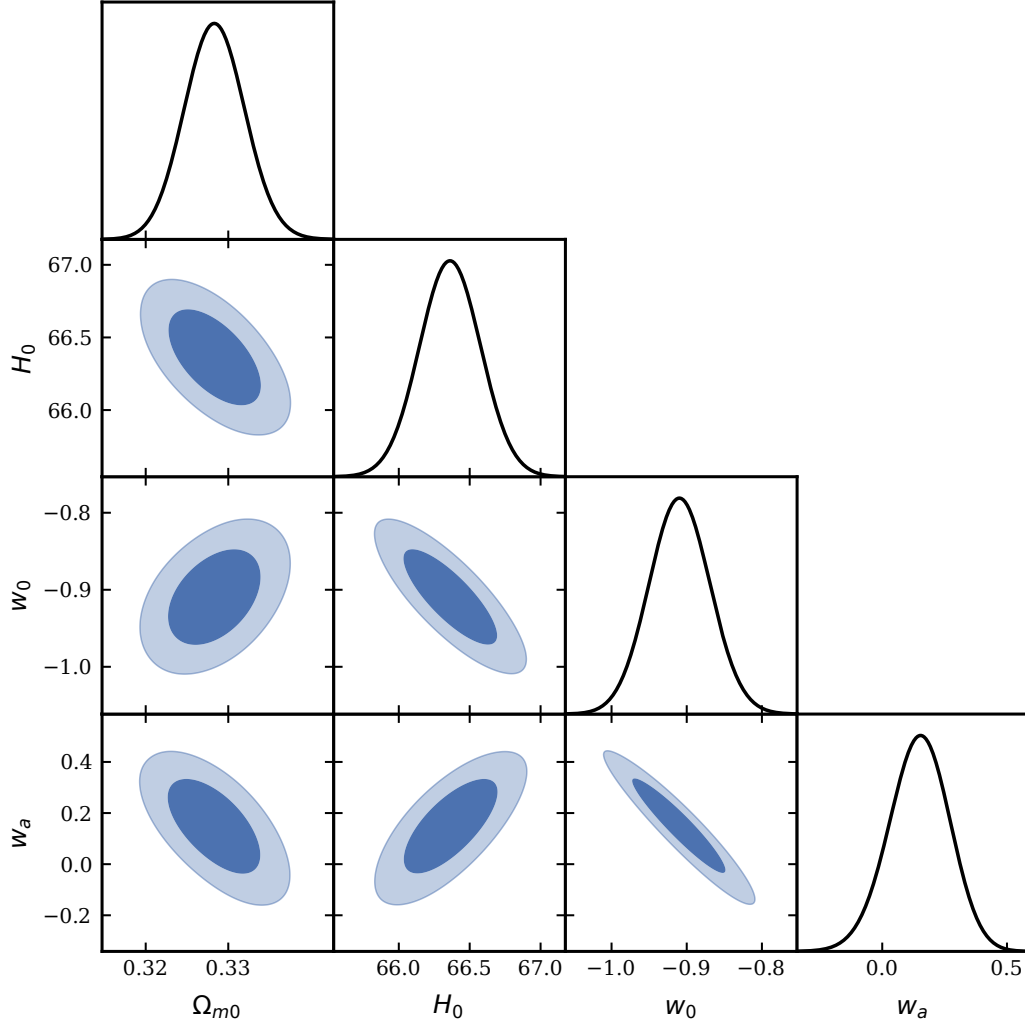


FIG. 2. **Run2 (SNe  $H_0 + 3\sigma$  tension).** Joint BAO+CMB+SNe posterior when the SNe zero-point is shifted by  $\Delta M = -0.09$ , mimicking a higher SNe-inferred Hubble constant. BAO and CMB remain fiducial. The contours move along the composite BAO+CMB degeneracy direction toward  $(\omega_0 > -1, \omega_a > 0)$ , demonstrating how a pure SNe calibration bias can generate an entirely spurious dynamical-DE signal.

$\Omega_{m0}$ -response direction so that the BAO-only likelihood attains its maximum near  $\Omega_{m0}^{(\text{BAO})} \simeq 0.28$ , two standard deviations below the fiducial value  $\Omega_{m0}^{(\text{fid})} = 0.30$ . No tensions are introduced in the CMB or SNe sectors, ensuring that the only cross-probe inconsistency present in run3 originates from the BAO-preferred matter density.

### 1. Posterior Shifts and Degeneracy Geometry

The median and  $1\sigma$  constraints from the joint BAO+CMB+SNe MCMC analysis are

$$\begin{aligned} \Omega_{m0} &= 0.2874^{+0.0035}_{-0.0034}, & H_0 &= 70.562^{+0.247}_{-0.251}, \\ \omega_0 &= -1.2012^{+0.0452}_{-0.0442}, & \omega_a &= 0.7412^{+0.1239}_{-0.1336}. \end{aligned} \quad (18)$$

These shifts reflect the characteristic imprint of a BAO-driven low- $\Omega_{m0}$  tension. The preferred matter density moves slightly below the fiducial value, while  $H_0$  shifts upward, lying between the CMB and SNe preferred directions. Most notably, the CPL parameters migrate into a strongly dynamical region, with  $\omega_0 < -1$  and  $\omega_a > 0$ , resembling a phantom-like form of DDE.

TABLE II. Qualitative degeneracy directions relevant for run3. The BAO sector is explicitly biased toward a lower matter density, while CMB and SNe remain fiducial. The joint shifts in Eq. (18) arise from the competition among these three misaligned ridge directions.

Probe	Dominant Degeneracy Direction	Physical Origin
BAO (biased)	$(\Omega_{m0} \downarrow, H_0 \uparrow, \omega_0 < -1, \omega_a > 0)$	Maintain $D_M/r_d, D_H/r_d$ under a reduced $\Omega_{m0}$
CMB (fiducial)	$(H_0 \downarrow, \omega_0 > -1, \omega_a > 0)$	Maintain consistency of $(R, \ell_A)$
SNe (fiducial)	$(H_0 \uparrow, \Omega_{m0} \downarrow)$	Shape of $\mu(z)$ with free absolute magnitude

This behaviour arises from the competition between the BAO-biased ridge direction and the orthogonal degeneracy structure of CMB and SNe. The BAO distortion pulls the BAO-only likelihood toward  $(\Omega_{m0} \downarrow, H_0 \uparrow)$ , a direction that also correlates with a tilt in the DE parameters toward  $(\omega_0 < -1, \omega_a > 0)$ . CMB distance priors, in contrast, stabilise the acoustic-scale combination  $(R, \ell_A)$  most effectively when  $H_0$  decreases and  $(\omega_0 > -1, \omega_a > 0)$ , while SNe prefer a nearly  $\Lambda$ CDM-like expansion history with  $(H_0 \uparrow, \Omega_{m0} \downarrow)$  in the presence of a free absolute magnitude. The joint posterior emerges from the compromise between these misaligned degeneracy directions, as summarised in Table II.

### 2. Tension-Injection Mechanism

The BAO tension in run3 is introduced by shifting the BAO-preferred matter density through a coherent distortion of the distance-ratio observables,  $d_1(z) \equiv D_M(z)/r_d$  and  $d_2(z) \equiv D_H(z)/r_d$ , along their response to  $\Omega_{m0}$ . Lowering  $\Omega_{m0}$  increases the comoving distance  $D_M(z)$  and decreases the expansion rate  $H(z)$  at the relevant BAO redshifts, producing correlated shifts in both  $D_M/r_d$  and  $D_H/r_d$ . Within the Fisher approximation, a small perturbation in the BAO-preferred matter density induces

$$\Delta d_i(z) \simeq \frac{\partial d_i}{\partial \Omega_{m0}} \Delta \Omega_{m0}^{(\text{BAO})}, \quad (19)$$

and we use this mapping to construct the distorted BAO mock. This ensures that the BAO-only posterior shifts along its natural ridge toward lower  $\Omega_{m0}$  without altering the internal covariance structure of the survey. The CMB and SNe likelihoods remain unmodified, so the only injected inconsistency is the BAO-preferred value  $\Omega_{m0}^{(\text{BAO})} \simeq 0.28$ . When the three probes are combined, the full likelihood

$$\mathcal{L}_{\text{tot}} = \mathcal{L}_{\text{BAO}}^{(\Omega_{m0}\text{-biased})} \mathcal{L}_{\text{CMB}}^{(\text{fid})} \mathcal{L}_{\text{SNe}}^{(\text{fid})} \quad (20)$$

must reconcile three misaligned degeneracy directions.

### 3. Pivot Equation-of-State

Recasting the CPL parameters in terms of the pivot EoS minimises the covariance between the DE amplitude and its slope. For run3, we obtain

$$a_p = 0.71, \quad z_p \simeq 0.41, \quad \omega_p = -1.045 \pm 0.018. \quad (21)$$

The pivot value lies moderately below  $-1$ , consistent with the phantom-like shift seen in  $(\omega_0, \omega_a)$ . For comparison, run2—where the injected tension resided entirely in the SNe sector—produced a pivot value above  $-1$ , corresponding to a quintessence-like trend. In contrast, run3 shows that shifting the BAO sector drives the pivot EoS below  $-1$ , illustrating that the direction of the apparent DE deviation is primarily determined by the probe in which the tension resides.

### 4. Joint Posterior Contours

Figure 3 presents the joint posterior for  $(\Omega_{m0}, H_0, \omega_0, \omega_a)$ . Relative to the tension-free baseline and the SNe-driven tension in run2, the  $(\omega_0, \omega_a)$  contours show a pronounced shift toward  $(\omega_0 < -1, \omega_a > 0)$ , consistent with the pivot trend in Eq. (21). In the  $(\Omega_{m0}, H_0)$  plane, the BAO-induced preference for lower  $\Omega_{m0}$  is only partially realised: CMB

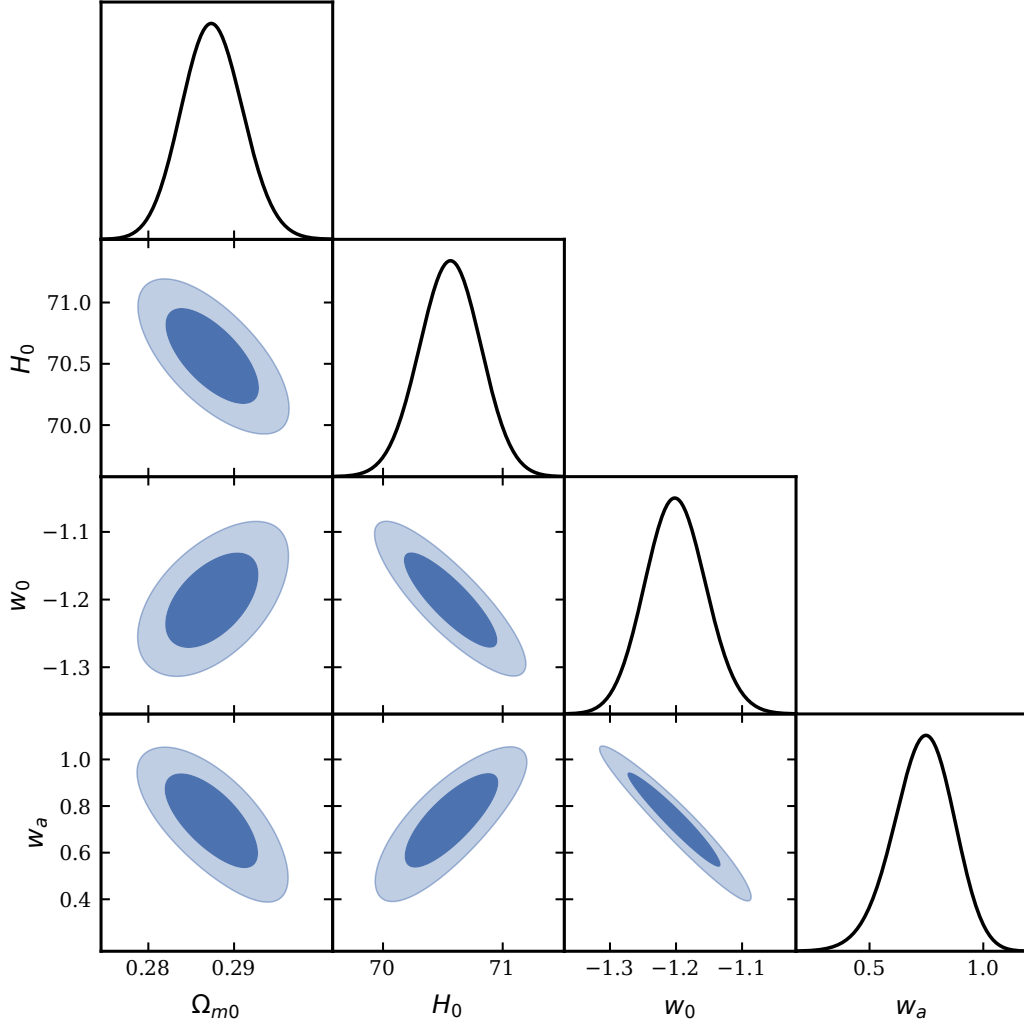


FIG. 3. **Run3 (BAO  $\Omega_{m0}$  tension).** Triangle plot from the joint BAO+CMB+SNe analysis. The BAO sector is biased toward a lower matter density, while the CMB and SNe mocks remain fiducial. The resulting posterior is displaced toward  $\Omega_{m0} \simeq 0.287$ ,  $H_0 \simeq 70.6$ , and  $(\omega_0, \omega_a) \simeq (-1.20, 0.74)$ , producing a strongly dynamical, phantom-like effective EoS, even though the underlying cosmology is exactly  $\Lambda$ CDM.

and SNe pull the matter density back upward toward 0.30. The compensation occurs primarily in the DDE direction rather than through shifts in  $H_0$ , since the BAO and CMB degeneracy directions intersect at shallow angles in the  $(\omega_0, \omega_a)$  plane. This makes the DDE parameters more efficient than  $H_0$  in reconciling the cross-probe inconsistency.

#### D. Run4: CMB Acoustic-Scale Tension via Low- $H_0$ Distance Prior

In run4 we introduce a controlled tension localized in the CMB sector, implemented as an effective shift in the CMB-preferred Hubble constant. The CMB mock is modified such that the distance-prior combination  $(R, \ell_A)$  favours a value of  $H_0^{(\text{CMB})} \simeq 65 \text{ km s}^{-1} \text{ Mpc}^{-1}$  which is approximately  $5 \text{ km s}^{-1} \text{ Mpc}^{-1}$  lower than the fiducial  $H_0^{(\text{fid})} = 70 \text{ km s}^{-1} \text{ Mpc}^{-1}$ . The BAO and SNe mocks remain fully fiducial ( $\Delta\Omega_{m0} = \Delta M = \Delta r_d = 0$ ), ensuring that the only cross-probe inconsistency in run4 originates from the CMB side through its low- $H_0$  preference [12, 69, 70]. This setup mimics a Planck-like acoustic-scale tension: lowering  $H_0$  while keeping  $r_d$  fixed increases the angular size of the sound horizon ( $\theta_s = r_d/D_A$ ), reproducing the characteristic direction of the CMB-local  $H_0$  discrepancy.

TABLE III. Qualitative degeneracy directions relevant for run4. Only the CMB mock is biased, favouring a lower  $H_0$ , while the BAO and SNe data remain fiducial. The interaction of these ridge directions determines the joint posterior structure in Eq. (22).

Probe	Dominant Degeneracy Direction	Physical Origin
CMB (biased)	$(H_0 \downarrow, \omega_0 < -1, \omega_a > 0)$	Maintain $(R, \ell_A)$ under reduced $H_0$
BAO (fiducial)	$(H_0 \downarrow, \Omega_{m0} \uparrow)$	Stabilise $D_M/r_d$ and $D_H/r_d$
SNe (fiducial)	$(H_0 \uparrow, \Omega_{m0} \downarrow)$	Geometry of $\mu(z)$ with free $M$

### 1. Posterior Shifts and Degeneracy Geometry

The median and  $1\sigma$  constraints obtained from the joint MCMC analysis are

$$\begin{aligned} \Omega_{m0} &= 0.3384 \pm 0.0031, & H_0 &= 69.875 \pm 0.166, \\ \omega_0 &= -1.1781 \pm 0.0166, & \omega_a &= 1.0822 \pm 0.0258. \end{aligned} \quad (22)$$

These shifts reflect the characteristic imprint of a CMB-driven low- $H_0$  tension. The inferred matter density increases well above the fiducial value, the resulting  $H_0$  lies slightly below 70, and the CPL parameters move deeply into the phantom-like region with  $\omega_0 < -1$  and  $\omega_a > 0$ . The strong excursion in  $(\omega_0, \omega_a)$  arises from the well-known sensitivity of the acoustic-scale combination  $(R, \ell_A)$  to changes in  $H_0$ : a lower  $H_0$  increases the sound-horizon angle  $\theta_s$ , which the MCMC partially compensates by shifting toward a late-time expansion history consistent with  $\omega_0 < -1$  and  $\omega_a > 0$ . The multi-probe geometry underlying these shifts is summarised in Table III. The biased CMB mock strongly prefers  $(H_0 \downarrow, \omega_0 < -1, \omega_a > 0)$ , while the fiducial BAO ridges favour  $(H_0 \downarrow, \Omega_{m0} \uparrow)$ , and the SNe degeneracy tends toward  $(H_0 \uparrow, \Omega_{m0} \downarrow)$ . The joint posterior aligns primarily with the BAO+CMB composite ridge, which links a decrease in  $H_0$  to simultaneous increases in  $\Omega_{m0}$  and a strong tilt toward  $(\omega_0 < -1, \omega_a > 0)$ . As in run3, the DE parameters absorb most of the inconsistency, but here the effect is substantially amplified due to the steep sensitivity of  $(R, \ell_A)$  to  $H_0$ .

### 2. Tension-Injection Mechanism

The CMB-side tension in run4 is introduced by modifying the distance-prior vector  $(R, \ell_A)$  so that it is internally consistent with a lower CMB-preferred Hubble parameter,

$$H_0^{(\text{CMB})} = H_0^{(\text{fid})} + \Delta H_0^{(\text{CMB})} = 70 - 5 \simeq 65 \text{ km s}^{-1} \text{ Mpc}^{-1}. \quad (23)$$

For fixed  $(\Omega_{m0}, \omega_0, \omega_a, r_d)$ , a decrease in  $H_0$  increases the sound-horizon angular scale  $\theta_s \equiv r_s(z_*)/D_A(z_*)$ , and hence shifts both the acoustic peak position  $\ell_A \propto \pi/\theta_s$  and the CMB shift parameter  $R = \sqrt{\Omega_{m0} H_0^2} D_M(z_*)$ . We implement the bias by mapping the fiducial distance-prior vector  $\mathbf{d}_{\text{CMB}}^{(\text{fid})} = (R_{\text{fid}}, \ell_{A,\text{fid}})$  to a shifted vector

$$\mathbf{d}_{\text{CMB}}^{(\text{biased})} = \mathbf{d}_{\text{CMB}}^{(\text{fid})} + \Delta \mathbf{d}_{\text{CMB}}, \quad (24)$$

where  $\Delta \mathbf{d}_{\text{CMB}}$  corresponds to the change induced when  $H_0$  is lowered by  $5 \text{ km s}^{-1} \text{ Mpc}^{-1}$  while keeping all other fiducial parameters fixed. In the Fisher approximation, this perturbation can be written as

$$\Delta d_i \simeq \frac{\partial d_i}{\partial H_0} \Delta H_0^{(\text{CMB})}, \quad d_i \in \{R, \ell_A\}, \quad (25)$$

ensuring that the CMB mock remains internally self-consistent but corresponds to a cosmology with a lower preferred Hubble constant.

No modifications are applied to the BAO or SNe sectors, so the full likelihood

$$\mathcal{L}_{\text{tot}} = \mathcal{L}_{\text{BAO}}^{(\text{fid})} \mathcal{L}_{\text{CMB}}^{(H_0\text{-biased})} \mathcal{L}_{\text{SNe}}^{(\text{fid})} \quad (26)$$

contains a single, well-defined inconsistency arising from the CMB acoustic scale. When combined with the BAO ridge (linking  $H_0 \downarrow$  to  $\Omega_{m0} \uparrow$ ) and the SNe ridge (linking  $H_0 \uparrow$  to  $\Omega_{m0} \downarrow$ ), the biased CMB priors force the joint solution toward the direction  $(H_0 \downarrow, \Omega_{m0} \uparrow, \omega_0 < -1, \omega_a > 0)$ , matching the behaviour observed in Eq. (22).

### 3. Pivot Equation-of-State

The pivot parameters extracted from the run4 posterior are

$$a_p = 1.0806, \quad z_p = -0.0746, \quad \omega_p = -1.2654 \pm 0.0186. \quad (27)$$

The negative value of  $z_p$  indicates that the pivot direction has rotated past  $z = 0$ , a clear sign that the CMB-induced tension forces the fit to compensate through rapid late-time evolution of the DE EoS. The pivot value lies far below  $-1$ , indicating a pronounced phantom-like behaviour driven almost entirely by the acoustic-scale inconsistency in the CMB sector. Compared with run3—which exhibited only a mild phantom-like shift—run4 demonstrates the substantially stronger tendency of the CMB acoustic scale to push the posterior toward  $\omega_0 < -1$  when  $H_0$  is artificially decreased.

### 4. Joint Posterior Contours

Figure 4 presents the joint posterior contours for  $(\Omega_{m0}, H_0, \omega_0, \omega_a)$  obtained in run4. The  $(\omega_0, \omega_a)$  ellipses are displaced far into the phantom-like quadrant, consistent with the pivot trend in Eq. (27), while the  $(\Omega_{m0}, H_0)$  contours reflect the combined BAO+CMB ridge that links lower  $H_0$  with higher  $\Omega_{m0}$ . Although the underlying cosmology is exactly  $\Lambda$ CDM, the CMB-side tension drives the combined posterior deeply into the DDE region.

## E. Run5: Opposite-Directed BAO–CMB Tensions

Run5 introduces two deliberately opposite-directed tensions in the BAO and CMB sectors [71, 72]. The BAO mock is distorted so that the BAO-only likelihood prefers a higher matter density,  $\Omega_{m0}^{(\text{BAO})} \simeq 0.33$ , while the CMB distance prior is modified to mimic a lower Hubble constant,  $H_0^{(\text{CMB})} \simeq 65$ . The SNe dataset remains strictly fiducial. This configuration generates the strongest mutual inconsistency among the tension scenarios studied here, with BAO and CMB pulling the parameters in nearly orthogonal directions within the  $(\Omega_{m0}, H_0, \omega_0, \omega_a)$  space. Run5 therefore constitutes a clean test of how conflicting degeneracy directions interfere when SNe are added as a third geometric anchor.

### 1. Posterior Shifts and Degeneracy Geometry

The median and  $1\sigma$  constraints obtained from the BAO+CMB+SNe MCMC analysis are

$$\begin{aligned} \Omega_{m0} &= 0.3371 \pm 0.0031, & H_0 &= 69.611 \pm 0.165, \\ \omega_0 &= -1.1533 \pm 0.0157, & \omega_a &= 1.0563 \pm 0.0228. \end{aligned} \quad (28)$$

The combined posterior reflects a coherent compromise between the competing BAO and CMB tension directions. The matter density shifts upward by roughly 12% relative to the fiducial value, dominated by the BAO-induced pull toward higher  $\Omega_{m0}$ , while the inferred Hubble constant decreases slightly below 70, moving toward the CMB-preferred low- $H_0$  direction. The CPL parameters respond to the combined BAO+CMB geometry by migrating into the  $(\omega_0 < -1, \omega_a > 0)$  quadrant associated with phantom-like evolution, but the shift is noticeably milder than in run4 because the BAO-side distortion partially counteracts the CMB-induced tilt.

Taken together, the three probes generate a highly non-parallel set of degeneracy directions as summarised in Table IV. The BAO bias drives the parameters toward  $(\Omega_{m0} \uparrow, H_0 \downarrow)$ , while the CMB bias enforces  $(H_0 \downarrow, \omega_0 < -1, \omega_a > 0)$ , and SNe remain centred on the fiducial  $(\Omega_{m0}, H_0)$  ridge. Because the BAO and CMB tensions pull the solution in nearly orthogonal directions in the  $(\Omega_{m0}, H_0, \omega_0, \omega_a)$  space, the resulting posterior corresponds to a vector-like compromise between these incompatible ridges. This yields the balanced displacement seen in Eq. (28), with a phantom-like shift that is substantially weaker than in run4 due to the partial cancellation of the BAO and CMB tension vectors.

### 2. Tension-Injection Mechanism

The BAO tension is implemented through a positive shift  $\Delta\Omega_{m0}^{(\text{BAO})} = +0.03$ , which modifies both  $D_M(z)/r_d$  and  $D_H(z)/r_d$  along their intrinsic sensitivity to the matter density. At fixed  $(H_0, \omega_0, \omega_a, r_d)$ , increasing  $\Omega_{m0}$  raises  $H(z)$

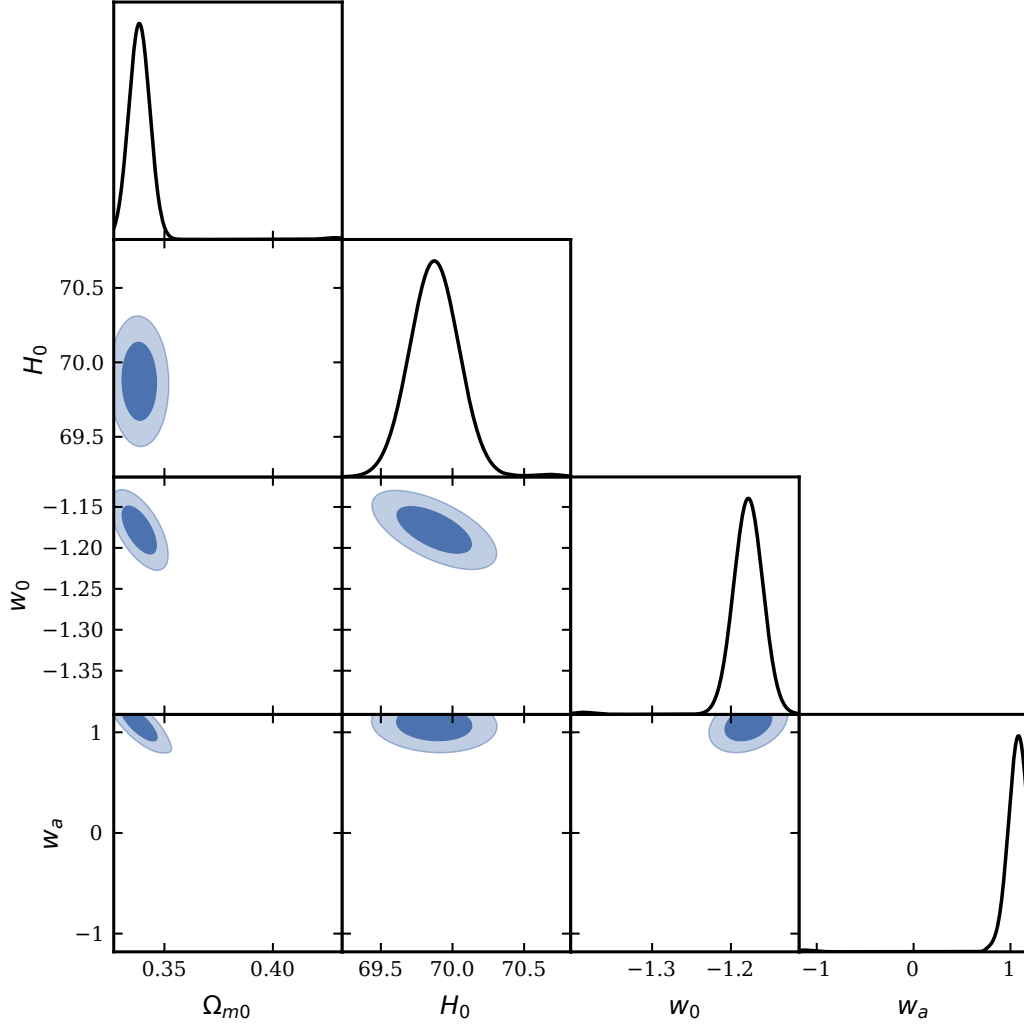


FIG. 4. **Run4 (CMB-side  $H_0$  / acoustic-scale tension).** Joint posterior for BAO+CMB+SNe when only the CMB mock is biased toward lower  $H_0$ . The resulting displacement toward  $\Omega_{m0} \simeq 0.338$ ,  $H_0 \simeq 69.9$ , and  $(\omega_0, \omega_a) \simeq (-1.18, 1.08)$  traces a steep, phantom-like degeneracy direction. This apparent DDE signature is produced entirely by the CMB side tension, despite the underlying cosmology being exactly  $\Lambda$ CDM.

TABLE IV. Qualitative degeneracy directions for run5. The BAO mock is biased toward high  $\Omega_{m0}$ , while the CMB mock is biased toward low  $H_0$ . The SNe sector remains fiducial. The joint posterior reflects a compromise between the nearly orthogonal tension directions.

Probe	Dominant Degeneracy Direction	Physical Origin
BAO (biased high $\Omega_{m0}$ )	$(\Omega_{m0} \uparrow, H_0 \downarrow)$	Maintain $D_M/r_d$ and $D_H/r_d$ at high $\Omega_{m0}$
CMB (biased low $H_0$ )	$(H_0 \downarrow, \omega_0 < -1, \omega_a > 0)$	Keep $(R, \ell_A)$ fixed under reduced $H_0$
SNe (fiducial)	$(H_0 \uparrow, \Omega_{m0} \downarrow)$	Luminosity-distance geometry with free $M$

and reduces  $D_M(z)$ , pulling the BAO-only posterior toward the high- $\Omega_{m0}$  region. Simultaneously, the CMB mock is adjusted via a negative shift in the preferred Hubble parameter,  $\Delta H_0^{(\text{CMB})} = -5 \text{ km s}^{-1} \text{ Mpc}^{-1}$ , which distorts the acoustic-scale variables  $(R, \ell_A)$  and shifts the CMB posterior toward  $(H_0 \downarrow, \omega_0 < -1, \omega_a > 0)$ . With SNe left fiducial, the full likelihood

$$\mathcal{L}_{\text{tot}} = \mathcal{L}_{\text{BAO}}^{(\Omega_{m0}\text{-biased})} \mathcal{L}_{\text{CMB}}^{(H_0\text{-biased})} \mathcal{L}_{\text{SNe}}^{(\text{fid})} \quad (29)$$



must reconcile three incompatible geometric ridges. The resulting solution is the balanced displacement visible in Eq. (28), lying between the BAO and CMB preferred directions. Importantly, the BAO-induced shift in  $(\Omega_{m0}, H_0)$  and the CMB-induced shift in  $(H_0, \omega_0, \omega_a)$  span nearly orthogonal directions in parameter space. This guarantees that the joint-posterior displacement is not dominated by either probe alone, but instead reflects the geometric interference between the two distinct tension vectors.

### 3. Pivot Equation-of-State

The pivot parameters for run5 are

$$a_p = 0.9628, \quad z_p = 0.0387, \quad \omega_p = -1.1143 \pm 0.0151. \quad (30)$$

The positive value of  $z_p$  indicates a pivot scale located slightly above the present epoch. The pivot EoS remains below  $-1$ , consistent with the phantom-like shift induced jointly by the BAO and CMB tensions, but the deviation from the fiducial value is significantly less extreme than in run4. This demonstrates how oppositely directed tension vectors can partially cancel, reducing the apparent severity of dynamical-DE behaviour in the pivot plane, despite the underlying cosmology being exactly  $\Lambda$ CDM. The relatively mild deviation of  $w_p$  from  $-1$ —especially compared with run4—highlights that opposite-directed tensions mitigate the severity of the apparent DDE signal. In this sense, run5 provides a clean demonstration that dynamical-DE-like posteriors can be either amplified or suppressed depending on the angular structure of the tension vectors in parameter space.

### 4. Joint Posterior Contours

Figure 5 displays the joint posterior contours for  $(\Omega_{m0}, H_0, \omega_0, \omega_a)$  in run5. The enhancement of  $\Omega_{m0}$  and the suppression of  $H_0$  produce a characteristic diagonal orientation in the  $(\omega_0, \omega_a)$  plane, reflecting the interference between BAO and CMB degeneracies. The elongation in  $\omega_a$  corresponds to the partial cancellation of the tension directions, which broadens the allowed region relative to run4.

## F. Run6: SNe Anchor Miscalibration (Zero-Point Shift)

A coherent shift in the SNe absolute magnitude is strictly degenerate with the Hubble constant [70, 73], yet its ability to bias cosmological parameters is tightly constrained when combined with high-redshift geometric probes via the inverse distance ladder [74, 75]. Run6 explicitly demonstrates this behaviour within our controlled tension-injection framework. In contrast to run2—which imposed a large, SH0ES-like negative  $\Delta M_B$  to enforce a strong high- $H_0$  preference—the perturbation applied here is deliberately subtle. This design isolates the intrinsic geometric sensitivity of the global BAO+CMB+SNe fit to SNe calibration errors, avoiding the strongly non-linear parameter distortions observed in runs 3–5.

### 1. Posterior Shifts and Degeneracy Geometry

The median and  $1\sigma$  constraints from the joint MCMC analysis are

$$\begin{aligned} \Omega_{m0} &= 0.2868 \pm 0.0033, & H_0 &= 71.048 \pm 0.237, \\ \omega_0 &= -1.0405 \pm 0.0427, & \omega_a &= 0.1097 \pm 0.1460. \end{aligned} \quad (31)$$

These shifts display the characteristic fingerprint of a SNe-only zero-point perturbation. The inferred Hubble constant moves slightly above the fiducial value, consistent with the SNe sector favoring a brighter absolute magnitude. Conversely, the matter density shifts mildly downward, following the correlation direction of the SNe ridge. The CPL parameters exhibit only a mild tilt toward  $(\omega_0 < -1, \omega_a > 0)$ , and the displacement is substantially smaller than in runs 3–5, reflecting the much weaker geometrical imprint of a small SNe-only calibration shift. This behaviour reflects the limited geometric leverage of SNe: a perturbation in  $\Delta M$  affects the global fit primarily through its degeneracy with  $H_0$ , and only secondarily through correlations with  $(\omega_0, \omega_a)$ .

The relevant degeneracy directions for each probe are summarised in Table V. The SNe distortion pushes the posterior toward  $(H_0 \uparrow, \Omega_{m0} \downarrow)$ , while the fiducial BAO and CMB likelihoods favour the opposing trends. The joint posterior therefore adopts an intermediate solution that remains very close to the fiducial expansion history.

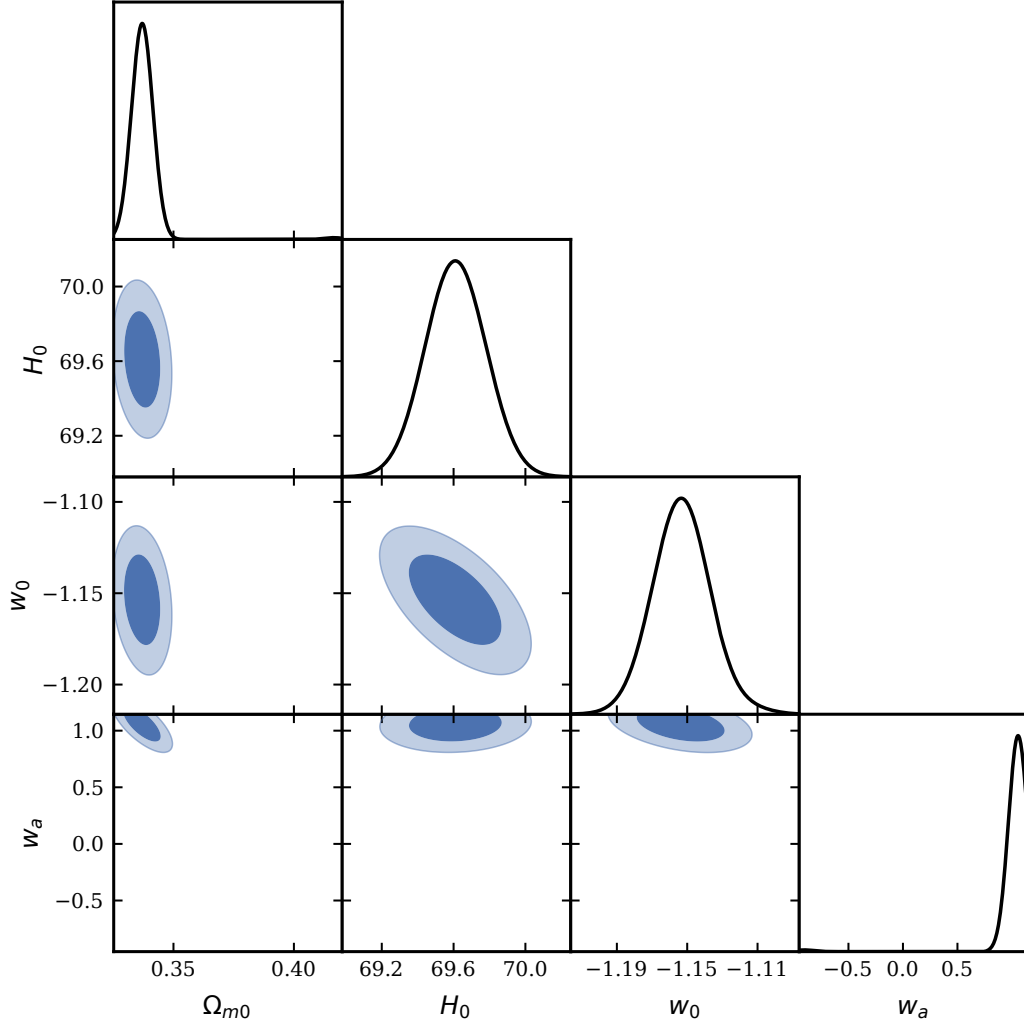


FIG. 5. **Run5 (opposite-directed BAO–CMB tensions).** Joint posterior for BAO+CMB+SNe when the BAO mock is biased toward high  $\Omega_{m0}$  and the CMB mock toward low  $H_0$ . The recovered parameters,  $\Omega_{m0} \simeq 0.337$ ,  $H_0 \simeq 69.6$ , and  $(\omega_0, \omega_a) \simeq (-1.15, 1.06)$ , reflect a compromise between mutually inconsistent ridge directions. The apparent DDE signature is weaker than in run4 due to the partial cancellation of BAO and CMB shifts.

TABLE V. Qualitative degeneracy directions for run6. Only the SNe distance scale is perturbed; BAO and CMB remain fiducial. The moderate shifts in Eq. (31) arise from the competition between the SNe ridge and the nearly orthogonal BAO and CMB degeneracies. The SNe ridge corresponds to the near-exact degeneracy between  $H_0$  and the SNe absolute magnitude, so its shifts primarily manifest as motions along the  $(H_0, \Omega_{m0})$  plane rather than in  $(\omega_0, \omega_a)$ .

Probe	Dominant Degeneracy Direction	Physical Origin
SNe (miscalibrated)	$(H_0 \uparrow, \Omega_{m0} \downarrow)$	Zero-point shift in $\mu(z)$
BAO (fiducial)	$(H_0 \downarrow, \Omega_{m0} \uparrow)$	Preserve $D_M/r_d$ and $D_H/r_d$
CMB (fiducial)	$(H_0 \downarrow, \omega_0 > -1, \omega_a > 0)$	Acoustic-scale consistency

## 2. Tension-Injection Mechanism

The SNe miscalibration is implemented by shifting the theoretical distance modulus from  $\mu_{\text{th}}(z)$  to  $\mu_{\text{th}}(z) + \Delta M$  with no changes applied to BAO or CMB. Since the distance module is given by

$$\mu = m - M = 5 \log_{10}(D_L/\text{Mpc}) + 25, \quad (32)$$

a brighter absolute magnitude ( $\Delta M < 0$ ) corresponds to a smaller inferred distance and hence a larger inferred value of  $H_0$  at fixed apparent magnitude. When the joint likelihood is evaluated, BAO and CMB counteract this trend by pulling toward lower  $H_0$ , resulting in the balanced shifts observed in Eq. (31). Because the imposed  $\Delta M$  is coherent across all redshifts, the SNe likelihood merely slides along its intrinsic  $(H_0, \Omega_{m0})$  degeneracy without altering its shape. The substantially higher constraining power of BAO and CMB therefore stabilizes the joint posterior, suppressing the impact of the SNe-only perturbation.

### 3. Pivot Equation-of-State

The pivot EoS parameters for run6 are

$$a_p = 0.7300, \quad z_p = 0.3699, \quad \omega_p = -1.0115 \pm 0.0153. \quad (33)$$

This remains essentially indistinguishable from  $\omega_p = -1$  within the statistical uncertainty, underscoring that a mild SNe zero-point offset has negligible impact on global DE constraints when BAO and CMB data are included. This sharply contrasts with the phantom-like pivots seen in runs 3–5, highlighting the significantly lower sensitivity of SNe calibration to the combined BAO+CMB geometry.

### 4. Joint Posterior Contours

Figure 6 displays the joint posterior for  $(\Omega_{m0}, H_0, \omega_0, \omega_a)$ . The contours show only modest displacements relative to the tension-free baseline. Most of the shift is confined to the  $(\Omega_{m0}, H_0)$  panel, tracing the shallow SNe ridge. BAO and CMB effectively stabilize the global fit, preventing the SNe miscalibration from producing any substantial deviation from  $\Lambda$ CDM.

## G. Run7: Combined Multi-Probe Systematic Tension

Run7 represents the most complex configuration in our controlled-tension suite. Unlike runs 2–6, which each introduce a single-probe inconsistency, run7 applies simultaneous but misaligned perturbations across the BAO and CMB sectors, while keeping the SNe dataset fiducial. This scenario is designed to emulate a realistic multi-probe environment in which BAO favour a slightly higher effective matter density, CMB prefer a lower Hubble constant, and SNe remain internally consistent. The resulting likelihood therefore contains mutually incompatible ridge directions, providing a clean test of how multi-probe conflicts propagate into apparent DDE [76, 77].

### 1. Posterior Shifts and Degeneracy Geometry

The median and  $1\sigma$  constraints from the joint MCMC analysis are

$$\begin{aligned} \Omega_{m0} &= 0.3246 \pm 0.0029, & H_0 &= 70.890 \pm 0.167, \\ \omega_0 &= -1.2054 \pm 0.0162, & \omega_a &= 1.1102 \pm 0.0238. \end{aligned} \quad (34)$$

Among all runs, run7 produces the most extreme departure from the fiducial  $\Lambda$ CDM values  $(0.30, 70, -1, 0)$ . The inferred matter density is significantly higher than the fiducial model, while  $H_0$  shifts moderately above 70. This counter-intuitive shift compensates for the accelerated expansion driven by the phantom EoS ( $\omega < -1$ ), which is required to match the CMB acoustic scale distance while simultaneously satisfying the biased BAO constraints. The CPL parameters exhibit a pronounced migration into the phantom-like quadrant ( $\omega_0 < -1, \omega_a > 1$ ), reflecting the absence of any consistent solution within the combined multi-probe degeneracy structure.

The underlying geometry of this displacement is summarised in Table VI. BAO, CMB, and SNe each prefer incompatible correlations in  $(\Omega_{m0}, H_0, \omega_0, \omega_a)$ , forcing the joint posterior into a region that satisfies none of the probes individually but lies along the only available escape direction in the CPL parameter space.

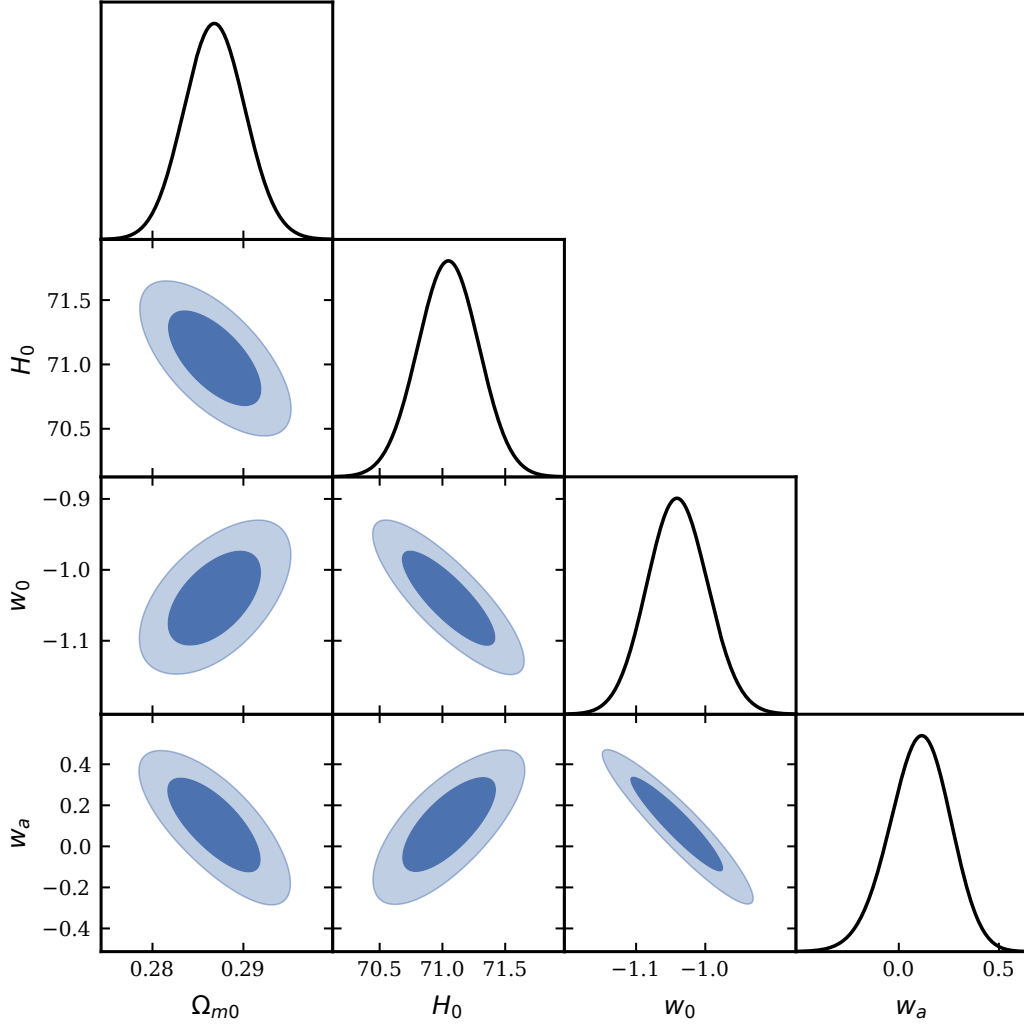


FIG. 6. **Run6 (SNe anchor miscalibration).** Joint BAO+CMB+SNe posterior when only the SNe zero point is shifted. The recovered parameters,  $\Omega_{m0} \simeq 0.287$ ,  $H_0 \simeq 71.0$ ,  $(w_0, w_a) \simeq (-1.04, 0.11)$ , and  $\omega_p \simeq -1.01$ , remain close to the fiducial  $\Lambda$ CDM cosmology. This illustrates the comparatively weak leverage of SNe-only miscalibration on the global DE constraints.

TABLE VI. Qualitative degeneracy directions relevant for run7. BAO favour higher  $\Omega_{m0}$ , CMB prefer lower  $H_0$ , while SNe remain fiducial. The severe misalignment among these directions produces the strongly phantom-like displacement in Eq. (34). Based on the degeneracy logic described in [12, 71].

Probe	Dominant Degeneracy Direction	Physical Origin
BAO (biased: $\Delta\Omega_{m0} > 0$ )	$(\Omega_{m0} \uparrow, H_0 \downarrow)$	Distorted $D_M/r_d$ , $D_H/r_d$ ratios
CMB (biased: $\Delta H_0 < 0$ )	$(H_0 \downarrow, w_0 > -1, w_a > 0)$	Maintain $(R, \ell_A)$ under low- $H_0$ shift
SNe (fiducial)	$(H_0 \uparrow, \Omega_{m0} \downarrow)$	Anchored expansion history

## 2. Tension-Injection Mechanism

The multi-probe tension in run7 is generated by combining two independent injections. First, a positive shift  $\Delta\Omega_{m0} > 0$  is applied to the BAO model predictions, producing directional distortions in both  $D_M(z)/r_d$  and  $D_H(z)/r_d$  that move the BAO-only posterior toward larger  $\Omega_{m0}$  and mildly lower  $H_0$ . Second, a negative shift  $\Delta H_0$  is applied to the CMB distance-prior vector  $(R, \ell_A)$ , mimicking a Planck-like low- $H_0$  preference. The SNe likelihood is kept completely fiducial, preserving its  $(H_0 \uparrow, \Omega_{m0} \downarrow)$  degeneracy.

The combined likelihood,

$$\mathcal{L}_{\text{tot}} = \mathcal{L}_{\text{BAO}}^{(\Delta\Omega_{m0}>0)} \mathcal{L}_{\text{CMB}}^{(\Delta H_0<0)} \mathcal{L}_{\text{SNe}}^{(\text{fid})},$$

must reconcile three incompatible ridge directions. Because no consistent solution exists at moderate  $(\Omega_{m0}, H_0)$ , the posterior is forced toward a rapidly evolving and strongly phantom-like EoS, as reflected by the values in Eq. (34).

### 3. Pivot Equation-of-State

The pivot quantities for run7 are

$$a_p = 0.3846, \quad z_p = 1.5999, \quad \omega_p = -0.5224 \pm 0.0067. \quad (35)$$

The extraordinarily high pivot redshift ( $z_p \simeq 1.6$ ) signals a severe rotation of the  $(\omega_0, \omega_a)$  degeneracy direction, far stronger than in any other run. Although the fundamental CPL parameters lie in the phantom regime, the pivot value moves into the opposite, quintessence-like region ( $\omega_p > -1$ )—a striking example of how strongly misaligned multi-probe tensions can cause qualitatively misleading interpretations of late-time DE behaviour. The exceptionally high pivot redshift originates from the extreme rotation of the  $(\omega_0, \omega_a)$  degeneracy direction induced by the simultaneous and mutually inconsistent tension channels active in run7. Because BAO, CMB, and SNe each impose nearly orthogonal ridge directions in the  $(\omega_0, \omega_a)$  plane, the combined posterior is forced into a direction that does not align with any individual probe. In the CPL parametrization, the pivot scale satisfies  $a_p = 1 + \text{Cov}(\omega_0, \omega_a)/\sigma_{\omega_a}^2$ , so a strong negative covariance—produced here by the geometrical interference of the three conflicting ridges—drives  $a_p$  far below unity, resulting in the extremely large value of  $z_p$ . This behaviour does not signal genuine high-redshift sensitivity to DE; rather, it reflects the breakdown of geometric coherence across the probes. The high pivot redshift is therefore a direct diagnostic of multi-probe inconsistency: the tension forces the CPL degeneracy direction to rotate so strongly that the inferred pivot moves into a regime where none of the probes individually have meaningful constraining power.

### 4. Joint Posterior Contours

Figure 7 shows the joint posterior for  $(\Omega_{m0}, H_0, \omega_0, \omega_a)$ . The displacement is the largest among all runs examined in this work. The  $(\Omega_{m0}, H_0)$  contours occupy a region that satisfies neither the BAO- nor the CMB-favoured direction individually, while the  $(\omega_0, \omega_a)$  contours extend deeply into the  $(\omega_0 < -1.2, \omega_a > 1.1)$  quadrant. This confirms that the multi-probe inconsistencies introduced in run7 produce a qualitative deformation of the CPL parameter space far exceeding any of the single-probe tensions previously examined.

## V. EMPIRICAL TENSION–BIAS TRANSFER FUNCTIONS

A central goal of this work is to construct an empirical mapping that links injected cross-probe tensions to the resulting cosmological parameter biases. Whereas the Fisher level expressions in Secs. VB theoretical origin of these mappings, relativistic likelihoods exhibit nonlinear and probe dependent degeneracy structures that require direct MCMC calibration. Using the controlled tension-injection runs (run2–run7), we construct a set of one-dimensional (1D) and two-dimensional (2D) empirical transfer functions. The 1D relations quantify the local linear response to isolated tension components. By contrast, the 2D maps capture the coupled effects of  $(\Delta\Omega_{m0}, \Delta H_0)$  tensions and reveal nonlinear behaviour that is absent in the 1D fits. Together, these empirical results form the backbone of the tension to bias forecasting framework developed in this paper.

### A. One-Dimensional Tension–Bias Relations

In this subsection we summarize simple one-dimensional fits that map injected tension parameters onto the resulting posterior biases in  $(\Omega_{m0}, H_0, \omega_0, \omega_a, \omega_p)$ , based on the controlled tension-injection runs (run2–run7).

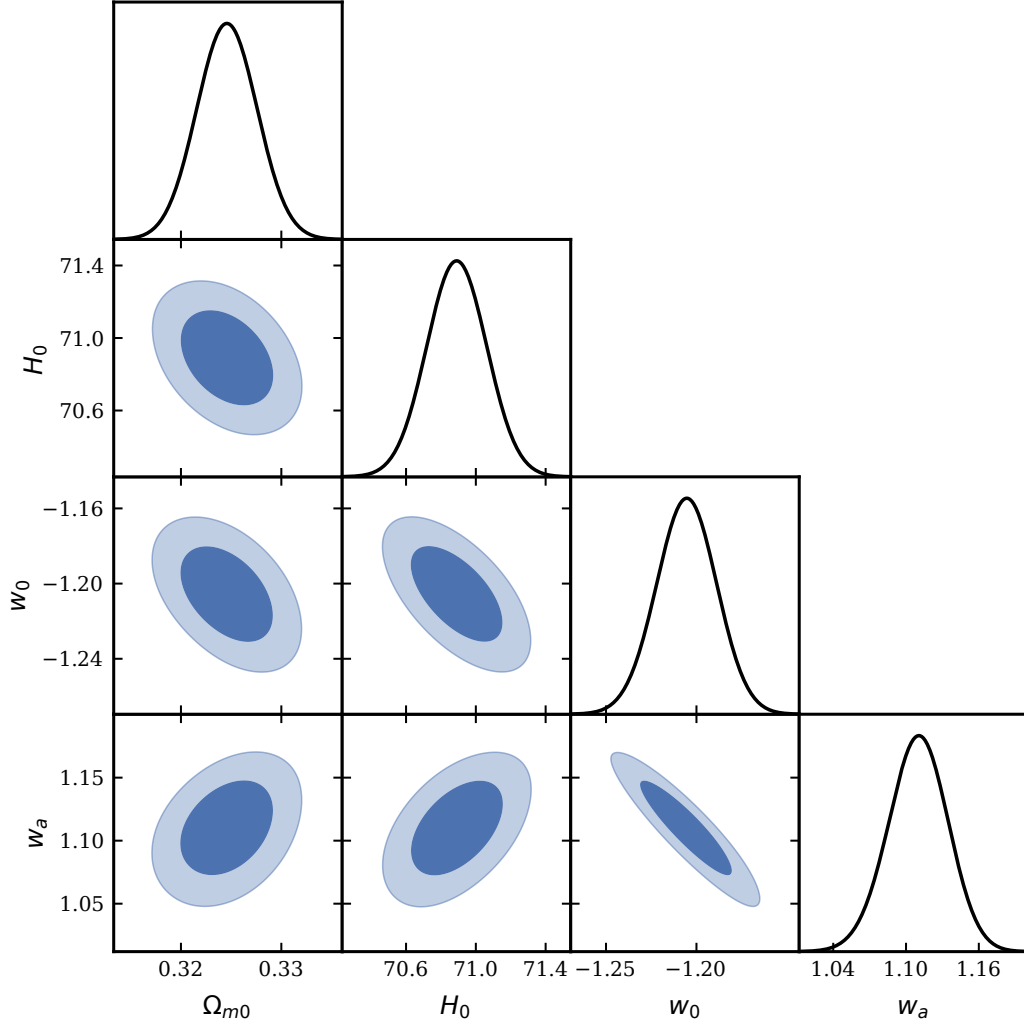


FIG. 7. **Run7 (combined multi-probe tension).** Joint BAO+CMB+SNe posterior when BAO are biased toward higher  $\Omega_{m0}$  and CMB toward lower  $H_0$ , with SNe fiducial. The conflicting ridge directions force the solution into the strongly dynamical, phantom-like region:  $\Omega_{m0} \simeq 0.325$ ,  $H_0 \simeq 70.9$ ,  $(\omega_0, \omega_a) \simeq (-1.21, 1.11)$ . The exceptionally large pivot redshift  $z_p \simeq 1.6$  reflects the extreme rotation of the CPL degeneracy unique to this run.

### 1. Tension in $\Omega_{m0}$

In this scenario we inject a controlled offset  $\Delta\Omega_{m0}$  and measure the resulting parameter shifts

$$\begin{aligned} \Delta\Omega_{m0}^{(\text{post})} &\simeq 0.9749 \Delta\Omega_{m0} + 1.0170 \times 10^{-2}, \Delta H_0^{(\text{post})} \simeq -1.1247 \times 10^1 \Delta\Omega_{m0} + 6.0557 \times 10^{-1}, \\ \Delta\omega_0 &\simeq 0.6533 \Delta\Omega_{m0} - 1.7934 \times 10^{-1}, \quad \Delta\omega_a \simeq 7.1200 \Delta\Omega_{m0} + 7.5432 \times 10^{-1}. \end{aligned} \quad (36)$$

### 2. Tension in $H_0$

Injecting a controlled offset  $\Delta H_0$  produces

$$\begin{aligned} \Delta\Omega_{m0}^{(\text{post})} &\simeq -3.6935 \times 10^{-3} \Delta H_0 + 1.8467 \times 10^{-2}, \Delta H_0^{(\text{post})} \simeq -2.6402 \times 10^{-2} \Delta H_0 + 1.3201 \times 10^{-1}, \\ \Delta\omega_0 &\simeq 1.6512 \times 10^{-2} \Delta H_0 - 8.2562 \times 10^{-2}, \quad \Delta\omega_a \simeq -9.3891 \times 10^{-2} \Delta H_0 + 4.6945 \times 10^{-1}. \end{aligned} \quad (37)$$

### 3. SNe absolute-magnitude tension

Injecting a SNe absolute-magnitude shift  $\Delta M$  yields

$$\begin{aligned}\Delta\Omega_{m0}^{(\text{post})} &\simeq -6.9189 \times 10^{-1} \Delta M - 3.0364 \times 10^{-2}, \quad \Delta H_0^{(\text{post})} \simeq 7.8093 \times 10^1 \Delta M + 3.5290, \\ \Delta\omega_0 &\simeq -2.1823 \Delta M - 9.2155 \times 10^{-2}, \quad \Delta\omega_a \simeq -6.8433 \times 10^{-1} \Delta M - 5.4823 \times 10^{-2}.\end{aligned}\quad (38)$$

#### B. From One-Dimensional Fits to a Multi-Dimensional Tension–Bias Map

The 1D relations above describe the response to single and isolated tension components. However, realistic analyses—such as DESI DR2 combined with Planck and SNe—generally involve multiple, correlated tensions. To accommodate such cases, we extend the 1D results into a multi-dimensional linear map.

$$\Delta\theta_{\text{post}} \simeq \mathbf{A} \Delta\mathbf{t}, \quad \Delta\mathbf{t} = (\Delta\Omega_{m0}, \Delta H_0, \Delta M)^\top, \quad \text{with} \quad \Delta\theta_{\text{post}} = (\Delta\Omega_{m0}^{\text{post}}, \Delta H_0^{\text{post}}, \Delta\omega_0, \Delta\omega_a)^\top. \quad (39)$$

##### 1. Construction of the Bias Matrix

Using the slopes in Eqs. (36)–(38), we obtain the  $4 \times 3$  empirical bias matrix

$$\mathbf{A} = \begin{pmatrix} 0.97493 & -3.6935 \times 10^{-3} & -0.69189 \\ -11.247 & -2.6402 \times 10^{-2} & 78.093 \\ 0.65334 & 1.6512 \times 10^{-2} & -2.1823 \\ 7.1200 & -9.3891 \times 10^{-2} & -0.68433 \end{pmatrix}. \quad (40)$$

##### 2. Two-Dimensional Bias Maps and Vector Diagrams

The linear relations summarized above characterize only the local, independent responses to single injected tensions. However, when multiple tension components are present simultaneously—as is common in DESI DR2, Planck, and SNe combinations—the resulting posterior biases in  $(\omega_0, \omega_a)$  need not follow the simple 1D slopes. In particular,  $\Delta\Omega_{m0}$  and  $\Delta H_0$  jointly distort the BAO and CMB likelihoods in a non-separable way, producing curved and anisotropic structures in the inferred DE parameters. To illustrate these multidimensional effects, we construct empirical 2D tension–bias maps for  $(\Delta\omega_0, \Delta\omega_a)$  using the full set of run2–run7 simulations.

Figure 8 shows the two empirical 2D tension–bias maps constructed directly from the run2–run7 sampling. Since each run corresponds to a distinct direction in the  $(\Delta\Omega_{m0}, \Delta H_0)$  plane, the morphology of the two maps is largely determined by how these six runs populate and distort the local neighbourhood around the origin. In the left panel, the curvature of  $\Delta\omega_0(\Delta\Omega_{m0}, \Delta H_0)$  arises from the interplay between BAO-oriented runs (run3 and run5), which shift the map along direction with shallow  $H_0$  variation, and  $H_0$ -dominated runs (run2 and run6), which steepen the vertical gradient. This superposition produces the diagonal warping seen in the contour lines. The combined effect produces the diagonal warping visible in the contour lines: the BAO-side runs populate the lower diagonal half of the map, whereas the CMB/SNe-like runs dominate the upper vertical region, leading to the characteristic deformation toward the  $D_H/r_d$  direction.

In the right panel, the map of  $\Delta\omega_a$  shows an even more nonlinear response. The pronounced curved ridge originates from the strong leverage of run2 and run6, both of which induce substantial effective shifts in the CMB acoustic angular scale and therefore project almost entirely onto the steep  $(\omega_0, \omega_a)$  degeneracy direction. Runs with primarily BAO-side tensions (run3 and run5) populate the left–right diagonal portion of the map, stretching the ridge along a direction consistent with the BAO constraint surface in the  $(\Omega_{m0}, H_0)$  plane. Because run7 combines BAO, CMB, and SNe tensions simultaneously, its influence appears as a smooth interpolation between these directions, further thickening the ridge and producing the nonlinear twist seen in the central region of the map.

Taken together, the two panels show that the full 2D structure of the tension–bias relationship arises from the superposition of the discrete run2–run7 tension directions. The BAO-dominated runs imprint a diagonal shear, the CMB/SNe-dominated runs imprint a nearly vertical distortion, and the mixed-tension run7 provides the curved interpolation between these axes. This explains why the resulting maps exhibit pronounced curvature and ridge-like anisotropies even in the nominally small-tension regime.

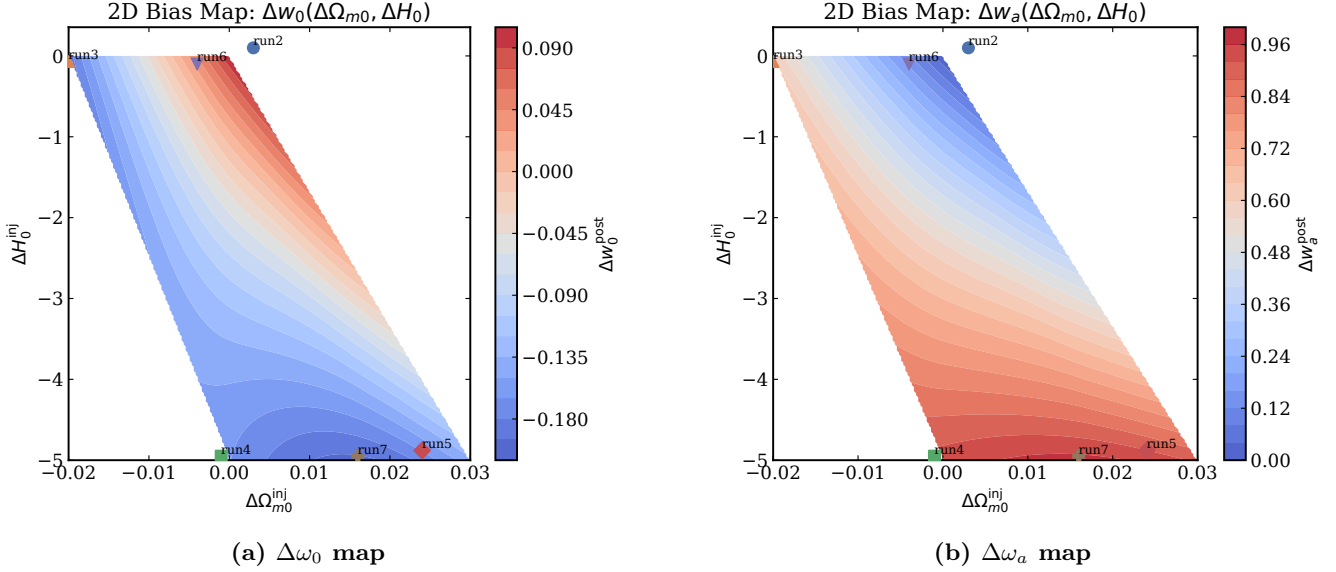


FIG. 8. Two-dimensional tension–bias maps for  $\Delta\omega_0$  and  $\Delta\omega_a$  as functions of the injected tensions  $(\Delta\Omega_{m0}, \Delta H_0)$ , constructed from run2–run7. Both panels show significant curvature and anisotropy, indicating nonlinear mixing of the tension directions even in the small-tension regime.

While the 2D maps reveal the local behaviour across the tension plane, the global distortion pattern becomes clearer when the responses are represented as normalized line segments in the  $(\omega_0, \omega_a)$  plane, as shown in Fig. 9. Each run contributes a directional line segment starting at the origin and ending at the normalized point  $(\Delta\omega_0, \Delta\omega_a)/\|(\Delta\omega_0, \Delta\omega_a)\|$ , with color and line style uniquely identifying the run. BAO-dominated runs (such as run3 and run5) produce line segments that lie nearly orthogonal to the CMB acoustic-scale degeneracy, whereas  $H_0$ -dominated runs (run2 and run6) are aligned with the steep CMB-preferred ridge, resulting in comparatively larger excursions in  $\Delta\omega_a$ . Run7 lies between these behaviours, reflecting the mild nonlinearity already visible in the 2D tension–bias maps. These patterns demonstrate that tension-induced distortions in DE parameter space are highly directional: cosmological constraints are intrinsically more sensitive to specific linear combinations of  $(\Delta\Omega_{m0}, \Delta H_0)$  than to either tension alone.

These combined results demonstrate that even modest cross-probe tensions generate a highly anisotropic response in  $(\omega_0, \omega_a)$ , with distinct ridge directions and nonlinear mixing between  $\Delta\Omega_{m0}$  and  $\Delta H_0$ . This behaviour directly motivates the multidimensional analysis in Sec. VC and explains why the 1D transfer functions systematically fail for large, realistic tensions such as those appearing in DESI DR2 + CMB.

### 3. Predicting Multi-Probe Biases

For any hypothetical tension vector  $\Delta\mathbf{t}$ , the predicted posterior shift follows directly from  $\Delta\boldsymbol{\theta}_{\text{post}} = \mathbf{A}\Delta\mathbf{t}$ . Conversely, given an observed shift  $\Delta\boldsymbol{\theta}_{\text{obs}}$ , the effective tension vector is

$$\Delta\mathbf{t}_{\text{eff}} \simeq (\mathbf{A}^\top \mathbf{A})^{-1} \mathbf{A}^\top \Delta\boldsymbol{\theta}_{\text{obs}}. \quad (41)$$

### C. Limitations of the One-Dimensional Transfer Functions

The one-dimensional tension–bias relations derived in the previous subsection offer a transparent and intuitive picture of how isolated tension components propagate into shifts of  $(\omega_0, \omega_a)$ . However, these relations are intrinsically local: they capture only the linear response of the posterior around the fiducial model and within the modest tension amplitudes explored in run2–run7. When applied to large or highly correlated tensions such as those observed in the DESI DR2 + CMB combination, the limitations of the 1D framework become immediately apparent.

To illustrate this breakdown concretely, consider the DESI DR2 + CMB deviations from the fiducial  $(0.30, 70, -1, 0)$ ,

$$\Delta\boldsymbol{\theta}_{\text{obs}} \simeq (+0.052, -6.3, +0.57, -1.70)^\top.$$



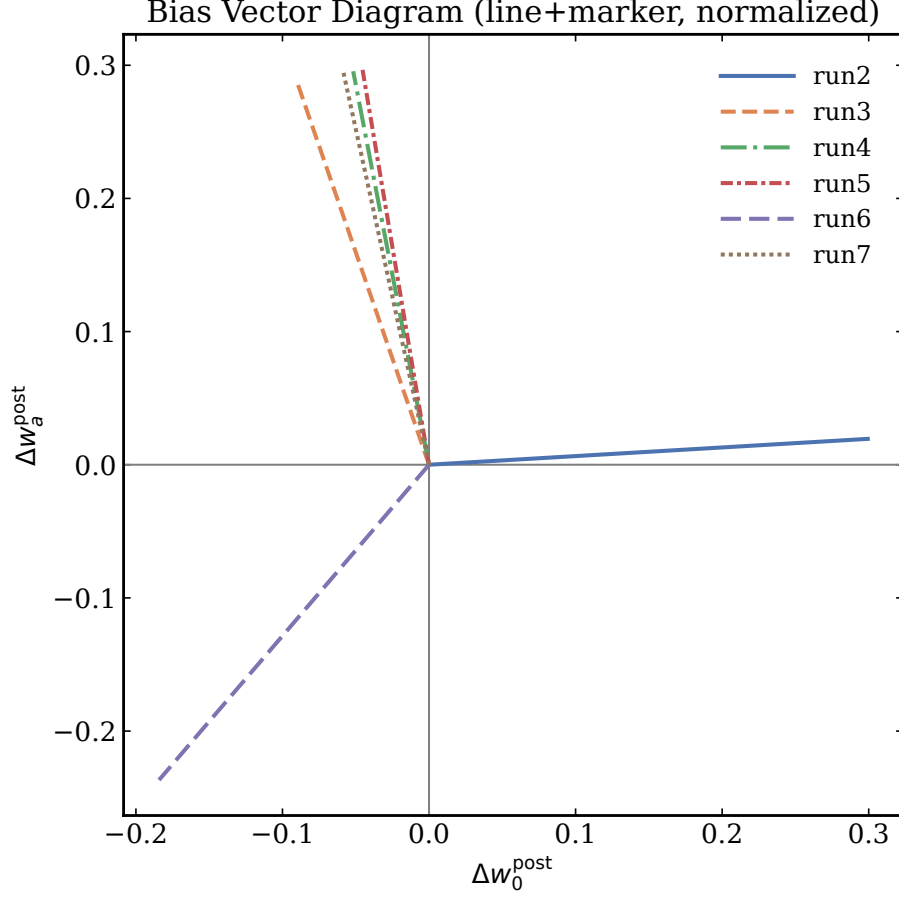


FIG. 9. Normalized bias vectors in the  $(\omega_0, \omega_a)$  plane for runs 2–7, plotted as line segments of unit length. Each segment originates at the origin and terminates at the normalized direction  $(\Delta\omega_0, \Delta\omega_a)/\|(\Delta\omega_0, \Delta\omega_a)\|$ . Runs are distinguished solely by colour and line style. The clustering of the segments along a small number of preferred orientations reflects the dominant roles of BAO radial-distance constraints and CMB acoustic-scale geometry in shaping tension-driven distortions in DE parameter space.

Using the empirical linear map of Eq. (41), we may infer the effective tensions required to reproduce these shifts. The resulting value,

$$\Delta\Omega_{m0}^{\text{inj}} \simeq +0.044, \quad \Delta H_0^{\text{inj}} \simeq -5.2 \text{ km s}^{-1} \text{ Mpc}^{-1}, \quad \Delta M^{\text{inj}} \approx 0,$$

correctly identifies the direction of the DESI–CMB discrepancy: a BAO-driven enhancement of  $\Omega_{m0}$  combined with a CMB-preferred suppression of  $H_0$ . Yet, when these inferred tensions are mapped back to the DE sector using the 1D relations, the predicted biases,

$$\Delta\omega_0^{\text{pred}} \approx -0.057, \quad \Delta\omega_a^{\text{pred}} \approx -0.175,$$

fall short by nearly an order of magnitude compared with the observed

$$\Delta\omega_0^{\text{obs}} \simeq +0.57, \quad \Delta\omega_a^{\text{obs}} \simeq -1.70.$$

This discrepancy is not a flaw of the method but rather a reflection of the fact that the 1D transfer functions were never designed to operate far from the fiducial region. Three physical effects underlie their breakdown. First, the calibration range of run2–run7 intentionally restricts the injected tensions to modest amplitudes, ensuring numerical stability and maintaining a locally linear response. Second, the CMB acoustic-scale likelihood possesses a strongly curved degeneracy direction in  $(\omega_0, \omega_a)$ : once the acoustic scale is displaced, beyond the local regime, the curvature

of this degeneracy ridge becomes dominant and the response ceases to be linear in  $(\Delta\Omega_{m0}, \Delta H_0)$ . Third, real CMB-side tensions are accompanied by correlated shifts in  $(r_d, \omega_b, n_s)$ , none of which are included in the minimal three-parameter tension vector  $(\Delta\Omega_{m0}, \Delta H_0, \Delta M)$ . The 1D framework cannot reproduce these coupled effects, and therefore it naturally underestimates large, nonlinear displacements.

Nevertheless, despite their limitations beyond the local regime, the 1D transfer functions remain highly valuable within the controlled-tension forecasting framework developed here. They provide an immediate and interpretable link between specific probe-level tensions and the resulting shifts in cosmological parameters, allowing one to identify which sector—BAO, CMB, or SNe—dominates the observed bias. More importantly, they offer a diagnostic baseline against which the fully nonlinear behaviour seen in 2D tension–bias maps or in real-data combinations can be quantified. The failure of the 1D approximation at large tensions is itself informative: it signals the onset of nonlinear mixing, identifies where curved degeneracy directions begin to dominate, and highlights the need for higher-order extensions such as global quadratic models, Fisher-bias corrections including covariance derivatives, or nonparametric Gaussian-process emulators trained on extended injection grids.

In this sense, the 1D relations are not a substitute for a full multi-dimensional treatment. Instead, they provide a conceptual anchor and a practical forecasting tool. They characterize the local structure of tension propagation, help diagnose departures from linear behaviour in real data, and guide the development of higher-order or emulator-based extensions of the tension to bias mapping.

## VI. DISCUSSION

The controlled tension–injection framework developed in this work clarifies how apparent hints of DDE can arise even when the underlying cosmology is exactly  $\Lambda$ CDM. By explicitly decoupling the origin of bias—the injected tension vector  $\Delta\mathbf{t}$ —from the statistical response of each probe, the framework provides a transparent interpretation of multi-probe inconsistencies that are otherwise difficult to diagnose.

Our simulations reveal three robust features of cross-probe tensions. First, BAO, CMB, and SNe respond differently to the same physical perturbation because they constrain distinct combinations of absolute and relative distance scales. A single tension such as  $\Delta H_0$  therefore induces nearly orthogonal shifts in the individual probes, and their intersections yield partial compensation rather than full cancellation. Residual misalignments in  $(\Omega_{m0}, H_0)$  then project onto the steep degeneracy directions of  $(\omega_0, \omega_a)$ , generating posterior shifts that resemble genuine DDE.

Second, Fisher-level linear predictions successfully reproduce the direction of these shifts across all scenarios, even when they underestimate the amplitude for larger tensions. This confirms that much of the DDE-like behaviour reported in recent multi-probe studies can be interpreted as the linear response of the posterior to mild cross-probe inconsistencies, rather than evidence for new physics.

Third, modest and observationally realistic tensions are already sufficient to displace the joint BAO+CMB+SNe posterior away from  $(\omega_0, \omega_a) = (-1, 0)$  at the  $1\text{--}2\sigma$  level. This highlights the importance of carefully synchronizing the absolute calibrations implicit in different probes before interpreting any deviation from  $\Lambda$ CDM as physical.

A particularly striking outcome appears in the multi-source tension scenario (run7). The CPL parameters  $(\omega_0, \omega_a)$  move into the phantom regime, yet the pivot parameter shifts to  $\omega_p \simeq -0.52$  at an anomalously high pivot redshift  $z_p \simeq 1.6$ . This occurs because strongly misaligned tension vectors force a rotation of the CPL degeneracy direction far beyond the region of data leverage. The result demonstrates that, under severe cross-probe inconsistencies, the pivot interpretation can become qualitatively misleading.

More broadly, the injection framework offers a systematic method for anticipating how next-generation analyses may respond to subtle calibration shifts, inconsistent priors, or redshift-dependent systematics. Because the approach is model-agnostic and fully simulation-based, it can be directly embedded in end-to-end pipelines to stress-test cosmological inferences in a controlled and reproducible manner.

## VII. CONCLUSION

We have introduced a controlled tension–injection framework that quantifies how probe–probe inconsistencies propagate into inferred dark-energy parameters. By parameterizing departures from mutual consistency in the BAO, CMB, and SNe sectors and tracing their impact through full MCMC analyses, the method cleanly separates the physical origin of bias (the tension vector  $\Delta\mathbf{t}$ ) from the statistical response of  $(\Omega_{m0}, H_0, \omega_0, \omega_a)$ .

Our results demonstrate that even modest cross-probe tensions can produce posterior shifts mimicking dynamical dark energy, including apparent exclusions of  $(\omega_0, \omega_a) = (-1, 0)$ , despite the underlying cosmology being exactly  $\Lambda$ CDM. The empirical 1D tension–bias relations provide reliable local diagnostics, while the 2D maps reveal nonlinear

mixing between tension components and identify the combinations of  $(\Delta\Omega_{m0}, \Delta H_0)$  to which dark energy constraints are most sensitive.

These findings underscore the importance of interpreting modern multi-probe analyses in light of how different datasets encode absolute and relative distance scales. The framework developed here offers a principled route to diagnosing apparent dynamical dark energy like signatures, assessing the robustness of the joint-probe constraints, and identifying which sectors of an analysis pipeline are most susceptible to tension-induced biases.

Looking ahead, the method is readily extendable to early dark energy, varying sound-horizon models, and modified-gravity frameworks, providing a systematic tool for distinguishing genuine new physics from artefacts of subtle cross-probe tensions in forthcoming precision surveys.

## Appendix A: Technical Supplement: Controlled Tension Injection and Fisher-Level Bias Propagation

This appendix summarizes the essential theoretical and methodological elements underlying the controlled tension-injection framework developed in the main text. Our aim is to provide a compact reference for the analytic structure of parameter biases, the construction of tension-modified likelihoods, and the interpretation of BAO, CMB, and SNe observables within Fisher theory. The material below complements, but does not repeat, the main discussion.

### 1. Science Rationale and Conceptual Goals

The controlled tension-injection project is designed to create a fully transparent environment in which cross-probe inconsistencies can be introduced and their impact on cosmological inference quantified. Within this framework, well-defined perturbations in parameters such as  $\Omega_{m0}$ ,  $H_0$ , the SNe absolute magnitude  $M$ , and the BAO sound horizon  $r_d$  are applied to otherwise self-consistent mocks. The resulting parameter shifts after running full likelihood analyses allow us to empirically map

$$\Delta\mathbf{t} \longrightarrow \Delta(\omega_0, \omega_a, \omega_p, \Omega_{m0}, H_0), \quad (\text{A1})$$

where  $\Delta\mathbf{t}$  denotes the injected tensions. These mappings form the backbone of the “tension  $\rightarrow$  bias” transfer functions employed throughout this work, and they provide practical guidance on how real-data inconsistencies propagate into apparent dark energy evolution.

### 2. Design of the Controlled Tension Pipeline

Tensions are introduced by modifying selected components of the data vector, priors, or mock generation procedure relative to a common fiducial  $\Lambda$ CDM cosmology. Typical cases include: (i) shifts in  $\Omega_{m0}$  motivated by BAO-SNe inconsistencies; (ii)  $H_0$  offsets mimicking SH0ES-Planck tension; (iii) zero-point or redshift-dependent calibration drifts in SNe; and (iv) changes in  $r_d$  or its effective value for BAO. Each tension is parametrized by control variables such as  $\Delta\Omega_{m0}$ ,  $\Delta H_0$ , or  $\Delta M$ , which can be scanned over a grid. For each injected configuration, MCMC analyses of individual or joint probe combinations are performed, and the resulting posterior shifts define the empirical tension-bias relations presented in the main text.

### 3. Fisher-Level Bias from SNe Calibration Drift

A subtle but important source of cross-probe tension arises from redshift-dependent evolution in the SNe Ia calibration. If the true absolute magnitude varies as

$$M_{\text{true}}(z) = M_0 + \Delta M_0 + \Delta M_1 z, \quad (\text{A2})$$

then the term proportional to  $z$  cannot be absorbed by a constant nuisance parameter  $M$  and inevitably induces biases in  $(\omega_0, \omega_a)$ . The resulting systematic residual in the Hubble diagram is

$$\Delta\mu(z_i) = \Delta M_0 + \Delta M_1 z_i, \quad (\text{A3})$$

and the linear tilt term sources a bias vector

$$b_\alpha^{(1)} = \Delta M_1 \sum_{i,j} \frac{\partial \mu(z_i)}{\partial \theta_\alpha} (C^{-1})_{ij} z_j, \quad (\text{A4})$$

for parameters  $\theta_\alpha \in \{\Omega_{m0}, H_0, \omega_0, \omega_a, M\}$ . The induced cosmological biases follow the standard Fisher expression,

$$\Delta \theta_\alpha = \sum_\beta (F^{-1})_{\alpha\beta} b_\beta, \quad (\text{A5})$$

with the tilt component projecting most strongly onto  $(\omega_0, \omega_a)$ . This formalism clarifies why even a mild calibration drift of order  $\Delta M_1 \sim 10^{-2}$  mag across  $z \sim 1$  can imitate an apparent evolution in the dark energy equation of state at the level  $\mathcal{O}(0.1)$ .

#### 4. Fisher-Level Bias from $\Delta\Omega_{m0}$ , $\Delta H_0$ , and $\Delta r_d$

Tensions in  $\Omega_{m0}$ ,  $H_0$ , and  $r_d$  arise frequently in joint analyses of DESI BAO, SNe, and CMB distance priors. If the theoretical model is displaced relative to the true cosmology by  $\Omega_{m0} \rightarrow \Omega_{m0} + \Delta\Omega_{m0}$ ,  $H_0 \rightarrow H_0 + \Delta H_0$ ,  $r_d \rightarrow r_d + \Delta r_d$ , then the induced residual in any probe's observable  $d_i$  takes the linearized form

$$\Delta d_i = -\frac{\partial d_i}{\partial \Omega_{m0}} \Delta\Omega_{m0} - \frac{\partial d_i}{\partial H_0} \Delta H_0 - \frac{\partial d_i}{\partial r_d} \Delta r_d. \quad (\text{A6})$$

The corresponding parameter bias is again determined by the Fisher-bias relation,

$$\Delta \theta_\alpha = -\sum_\beta (F^{-1})_{\alpha\beta} \left[ \Delta\Omega_{m0} S_\beta^{(\Omega)} + \Delta H_0 S_\beta^{(H)} + \Delta r_d S_\beta^{(r_d)} \right], \quad (\text{A7})$$

where the projection coefficients  $S_\beta^{(X)}$  encode how each probe transmits a given tension into the CPL parameter space. These analytic expressions provide a convenient theoretical reference for interpreting the empirical 2D bias maps of the main text and help explain the differing pathways through which BAO, CMB, and SNe propagate the same physical tension.

#### 5. Analytic Derivatives for DESI BAO and CMB Distance Priors

For completeness, we summarize the derivatives entering the Fisher-level expressions. The DESI BAO observables,  $d_1(z) = D_M(z)/r_d$ ,  $d_2(z) = D_H(z)/r_d$ , yield the simple  $r_d$  derivative

$$\frac{\partial d_{1,2}}{\partial r_d} = -\frac{d_{1,2}}{r_d}, \quad (\text{A8})$$

while derivatives with respect to  $\Omega_{m0}$  involve  $\partial H(z)/\partial \Omega_{m0}$  and its effect on  $D_M(z)$  through line-of-sight integration. Likewise, for the CMB distance priors  $(R, \ell_A)$ , the relevant derivatives combine  $\partial D_M(z_*)/\partial \theta$  and  $\partial r_s(z_*)/\partial \theta$ , with their propagation into

$$R = \sqrt{\Omega_{m0}} H_0 D_M(z_*)/c, \quad \ell_A = \pi D_M(z_*)/r_s(z_*). \quad (\text{A9})$$

These derivatives determine how perturbations in early-time or late-time parameters shift the acoustic scale and distance ratio constraints in CMB+BAO joint analyses.

#### 6. Forecasting Workflow

The forecasting pipeline proceeds by generating fiducial BAO, CMB, and SNe mocks; introducing controlled tensions in selected parameters; running MCMC analyses on individual and combined probes; and quantifying the induced parameter shifts. The resulting displacements in  $(\Omega_{m0}, H_0, \omega_0, \omega_a, \omega_p)$  as functions of the injected tension parameters provide the empirical tension-bias transfer functions used throughout the main text. These relations allow one to interpret real-data inconsistencies in a controlled, quantitative manner and form the foundation of the predictive framework developed in this work.

## ACKNOWLEDGMENTS

This work is supported by Basic Science Research Program through the National Research Foundation of Korea (NRF) funded by the Ministry of Science and ICT under the Grants No. NRF-RS-2021-NR059413.

- 
- [1] A. G. Adame *et al.* [DESI], JCAP **02**, 021 (2025) doi:10.1088/1475-7516/2025/02/021 [arXiv:2404.03002 [astro-ph.CO]].
  - [2] M. Abdul Karim *et al.* [DESI], Phys. Rev. D **112**, no.8, 083515 (2025) doi:10.1103/tr6y-kpc6 [arXiv:2503.14738 [astro-ph.CO]].
  - [3] K. Lodha *et al.* [DESI], Phys. Rev. D **112**, no.8, 083511 (2025) doi:10.1103/w4c6-1r5j [arXiv:2503.14743 [astro-ph.CO]].
  - [4] S. R. Brownsberger, D. Brout, D. Scolnic, C. W. Stubbs and A. G. Riess, Astrophys. J. **944**, no.2, 188 (2023) doi:10.3847/1538-4357/acad80 [arXiv:2110.03486 [astro-ph.CO]].
  - [5] D. Scolnic, D. Brout, A. Carr, A. G. Riess, T. M. Davis, A. Dwomoh, D. O. Jones, N. Ali, P. Charvu and R. Chen, *et al.* Astrophys. J. **938**, no.2, 113 (2022) doi:10.3847/1538-4357/ac8b7a [arXiv:2112.03863 [astro-ph.CO]].
  - [6] D. Brout, G. Taylor, D. Scolnic, C. M. Wood, B. M. Rose, M. Vincenzi, A. Dwomoh, C. Lidman, A. Riess and N. Ali, *et al.* Astrophys. J. **938**, no.2, 111 (2022) doi:10.3847/1538-4357/ac8bcc [arXiv:2112.03864 [astro-ph.CO]].
  - [7] D. Brout, D. Scolnic, B. Popovic, A. G. Riess, J. Zuntz, R. Kessler, A. Carr, T. M. Davis, S. Hinton and D. Jones, *et al.* Astrophys. J. **938**, no.2, 110 (2022) doi:10.3847/1538-4357/ac8e04 [arXiv:2202.04077 [astro-ph.CO]].
  - [8] Z. G. Lane, A. Seifert, R. Ridden-Harper and D. L. Wiltshire, Mon. Not. Roy. Astron. Soc. **536**, no.2, 1752-1777 (2025) doi:10.1093/mnras/stae2437 [arXiv:2311.01438 [astro-ph.CO]].
  - [9] M. Vincenzi *et al.* [DES], Mon. Not. Roy. Astron. Soc. **541**, no.3, 2585-2593 (2025) doi:10.1093/mnras/staf943 [arXiv:2501.06664 [astro-ph.CO]].
  - [10] P. A. R. Ade *et al.* [Planck], Astron. Astrophys. **571**, A16 (2014) doi:10.1051/0004-6361/201321591 [arXiv:1303.5076 [astro-ph.CO]].
  - [11] N. Aghanim *et al.* [Planck], Astron. Astrophys. **641**, A6 (2020) [erratum: Astron. Astrophys. **652**, C4 (2021)] doi:10.1051/0004-6361/201833910 [arXiv:1807.06209 [astro-ph.CO]].
  - [12] L. Chen, Q. G. Huang and K. Wang, JCAP **02**, 028 (2019) doi:10.1088/1475-7516/2019/02/028 [arXiv:1808.05724 [astro-ph.CO]].
  - [13] Z. Zhai, C. G. Park, Y. Wang and B. Ratra, JCAP **07**, 009 (2020) doi:10.1088/1475-7516/2020/07/009 [arXiv:1912.04921 [astro-ph.CO]].
  - [14] P. Lemos and A. Lewis, Phys. Rev. D **107**, no.10, 103505 (2023) doi:10.1103/PhysRevD.107.103505 [arXiv:2302.12911 [astro-ph.CO]].
  - [15] I. D. Gialamas, G. Hütsi, K. Kannike, A. Racioppi, M. Raidal, M. Vasar and H. Veermäe, Phys. Rev. D **111**, no.4, 043540 (2025) doi:10.1103/PhysRevD.111.043540 [arXiv:2406.07533 [astro-ph.CO]].
  - [16] S. Roy Choudhury and T. Okumura, Astrophys. J. Lett. **976**, no.1, L11 (2024) doi:10.3847/2041-8213/ad8c26 [arXiv:2409.13022 [astro-ph.CO]].
  - [17] Z. Lu, T. Simon and P. Zhang, [arXiv:2503.04602 [astro-ph.CO]].
  - [18] B. R. Dinda, R. Maartens, S. Saito and C. Clarkson, JCAP **08**, 018 (2025) doi:10.1088/1475-7516/2025/08/018 [arXiv:2504.09681 [astro-ph.CO]].
  - [19] M. Scherer, M. A. Sabogal, R. C. Nunes and A. De Felice, Phys. Rev. D **112**, no.4, 043513 (2025) doi:10.1103/n86r-sjgm [arXiv:2504.20664 [astro-ph.CO]].
  - [20] M. A. Sabogal and R. C. Nunes, JCAP **09**, 084 (2025) doi:10.1088/1475-7516/2025/09/084 [arXiv:2505.24465 [astro-ph.CO]].
  - [21] I. D. Gialamas, G. Hütsi, M. Raidal, J. Urrutia, M. Vasar and H. Veermäe, Phys. Rev. D **112**, no.6, 063551 (2025) doi:10.1103/kdqc-y37v [arXiv:2506.21542 [astro-ph.CO]].
  - [22] S. Dhawan and E. Mörtzell, [arXiv:2506.22599 [astro-ph.CO]].
  - [23] E. Silva and R. C. Nunes, JCAP **11**, 078 (2025) doi:10.1088/1475-7516/2025/11/078 [arXiv:2507.13989 [astro-ph.CO]].
  - [24] M. Ishak and L. Medina-Varela, [arXiv:2507.22856 [astro-ph.CO]].
  - [25] J. Q. Wang, R. G. Cai, Z. K. Guo and S. J. Wang, [arXiv:2508.01759 [astro-ph.CO]].
  - [26] S. Roy Choudhury, T. Okumura and K. Umetsu, Astrophys. J. Lett. **994**, no.1, L26 (2025) doi:10.3847/2041-8213/ae1a64 [arXiv:2509.26144 [astro-ph.CO]].
  - [27] W. Giarè, M. Najafi, S. Pan, E. Di Valentino and J. T. Firouzjaee, JCAP **10**, 035 (2024) doi:10.1088/1475-7516/2024/10/035 [arXiv:2407.16689 [astro-ph.CO]].
  - [28] A. Notari, M. Redi and A. Tesi, JCAP **04**, 048 (2025) doi:10.1088/1475-7516/2025/04/048 [arXiv:2411.11685 [astro-ph.CO]].
  - [29] T. M. C. Abbott *et al.* [DES], [arXiv:2503.06712 [astro-ph.CO]].
  - [30] D. D. Y. Ong, D. Yallup and W. Handley, [arXiv:2511.10631 [astro-ph.CO]].
  - [31] D. Shlivko and P. J. Steinhardt, Phys. Lett. B **855**, 138826 (2024) doi:10.1016/j.physletb.2024.138826 [arXiv:2405.03933 [astro-ph.CO]].
  - [32] W. Giarè, T. Mahassen, E. Di Valentino and S. Pan, Phys. Dark Univ. **48**, 101906 (2025) doi:10.1016/j.dark.2025.101906 [arXiv:2502.10264 [astro-ph.CO]].

- [33] T. L. Smith, M. Lucca, V. Poulin, G. F. Abellan, L. Balkenhol, K. Benabed, S. Galli and R. Murgia, *Phys. Rev. D* **106**, no.4, 043526 (2022) doi:10.1103/PhysRevD.106.043526 [arXiv:2202.09379 [astro-ph.CO]].
- [34] V. Poulin, T. L. Smith and T. Karwal, *Phys. Dark Univ.* **42**, 101348 (2023) doi:10.1016/j.dark.2023.101348 [arXiv:2302.09032 [astro-ph.CO]].
- [35] G. Efstathiou, *Mon. Not. Roy. Astron. Soc.* **538**, no.2, 875-882 (2025) doi:10.1093/mnras/staf301 [arXiv:2408.07175 [astro-ph.CO]].
- [36] E. Ó. Colgáin and M. M. Sheikh-Jabbari, *Mon. Not. Roy. Astron. Soc.* **542**, no.1, L24-L30 (2025) doi:10.1093/mnras/slaf042 [arXiv:2412.12905 [astro-ph.CO]].
- [37] E. Di Valentino *et al.* [CosmoVerse Network], *Phys. Dark Univ.* **49**, 101965 (2025) doi:10.1016/j.dark.2025.101965 [arXiv:2504.01669 [astro-ph.CO]].
- [38] S. Lee, *Mon. Not. Roy. Astron. Soc.* **544**, 3388-3393 (2025) doi:10.1093/mnras/staf1890 [arXiv:2506.16022 [astro-ph.CO]].
- [39] R. Camilleri *et al.* [DES], *Mon. Not. Roy. Astron. Soc.* **533**, no.3, 2615-2639 (2024) doi:10.1093/mnras/stae1988 [arXiv:2406.05048 [astro-ph.CO]].
- [40] M. Chevallier and D. Polarski, *Int. J. Mod. Phys. D* **10**, 213 (2001) doi:10.1142/S0218271801000822 [arXiv:gr-qc/0009008].
- [41] E. V. Linder, *Phys. Rev. Lett.* **90**, 091301 (2003) doi:10.1103/PhysRevLett.90.091301 [arXiv:astro-ph/0208512].
- [42] L. Huang, R. G. Cai and S. J. Wang, *Sci. China Phys. Mech. Astron.* **68**, no.10, 100413 (2025) doi:10.1007/s11433-025-2754-5 [arXiv:2502.04212 [astro-ph.CO]].
- [43] S. Lee, [arXiv:2511.16703 [astro-ph.CO]].
- [44] C. Clarkson and R. Maartens, *Class. Quant. Grav.* **27**, 124008 (2010) doi:10.1088/0264-9381/27/12/124008 [arXiv:1005.2165 [astro-ph.CO]].
- [45] W. Handley and P. Lemos, *Phys. Rev. D* **100**, no.4, 043504 (2019) doi:10.1103/PhysRevD.100.043504 [arXiv:1902.04029 [astro-ph.CO]].
- [46] A. Heavens, Y. Fantaye, E. Sellentin, H. Eggers, Z. Hosenie, S. Kroon and A. Mootoovaloo, *Phys. Rev. Lett.* **119**, no.10, 101301 (2017) doi:10.1103/PhysRevLett.119.101301 [arXiv:1704.03467 [astro-ph.CO]].
- [47] E. Di Valentino, O. Mena, S. Pan, L. Visinelli, W. Yang, A. Melchiorri, D. F. Mota, A. G. Riess and J. Silk, *Class. Quant. Grav.* **38**, no.15, 153001 (2021) doi:10.1088/1361-6382/ac086d [arXiv:2103.01183 [astro-ph.CO]].
- [48] C. L. Steinhardt, P. Phillips and R. Wojtak, [arXiv:2504.03829 [astro-ph.CO]].
- [49] X. T. Tang, D. Brout, T. Karwal, C. Chang, V. Miranda and M. Vincenzi, *Astrophys. J. Lett.* **983**, no.1, L27 (2025) doi:10.3847/2041-8213/adc4da [arXiv:2412.04430 [astro-ph.CO]].
- [50] S. Lee, [arXiv:2507.01380 [astro-ph.CO]].
- [51] A. Albrecht, G. Bernstein, R. Cahn, W. L. Freedman, J. Hewitt, W. Hu, J. Huth, M. Kamionkowski, E. W. Kolb and L. Knox, *et al.* [arXiv:astro-ph/0609591 [astro-ph]].
- [52] D. Huterer and A. Cooray, *Phys. Rev. D* **71**, 023506 (2005) doi:10.1103/PhysRevD.71.023506 [arXiv:astro-ph/0404062 [astro-ph]].
- [53] D. Martin and A. Albrecht, [arXiv:astro-ph/0604401 [astro-ph]].
- [54] D. Scovacricchi, S. A. Bonometto, M. Mezzetti and G. La Vacca, *New Astron.* **26**, 106-111 (2014) doi:10.1016/j.newast.2013.07.005 [arXiv:1211.7315 [astro-ph.CO]].
- [55] S. Lee, [arXiv:2506.18230 [astro-ph.CO]].
- [56] J. Zhang, R. An, S. Liao, W. Luo, Z. Li and B. Wang, *Phys. Rev. D* **98**, no.10, 103530 (2018) doi:10.1103/PhysRevD.98.103530 [arXiv:1811.01519 [astro-ph.CO]].
- [57] N. Jeffrey *et al.* [DES], *Mon. Not. Roy. Astron. Soc.* **536**, no.2, 1303-1322 (2024) doi:10.1093/mnras/stae2629 [arXiv:2403.02314 [astro-ph.CO]].
- [58] S. Afroz and S. Mukherjee, [arXiv:2504.16868 [astro-ph.CO]].
- [59] C. Duangchan, A. Valade, N. I. Libeskind and M. Steinmetz, [arXiv:2507.22236 [astro-ph.CO]].
- [60] A. Abate *et al.* [LSST Dark Energy Science], doi:10.2172/1156445 [arXiv:1211.0310 [astro-ph.CO]].
- [61] E. Allys *et al.* [LiteBIRD], *PTEP* **2023**, no.4, 042F01 (2023) doi:10.1093/ptep/ptac150 [arXiv:2202.02773 [astro-ph.IM]].
- [62] P. Ade *et al.* [Simons Observatory], *JCAP* **02**, 056 (2019) doi:10.1088/1475-7516/2019/02/056 [arXiv:1808.07445 [astro-ph.CO]].
- [63] M. Tegmark, *Astrophys. J. Lett.* **480**, L87-L90 (1997) doi:10.1086/310631 [arXiv:astro-ph/9611130 [astro-ph]].
- [64] C. B. Morrison and M. D. Schneider, *JCAP* **11**, 009 (2013) doi:10.1088/1475-7516/2013/11/009 [arXiv:1304.7789 [astro-ph.CO]].
- [65] D. Wadekar, M. M. Ivanov and R. Scoccimarro, *Phys. Rev. D* **102**, 123521 (2020) doi:10.1103/PhysRevD.102.123521 [arXiv:2009.00622 [astro-ph.CO]].
- [66] D. Foreman-Mackey, D. W. Hogg, D. Lang and J. Goodman, *Publ. Astron. Soc. Pac.* **125**, 306-312 (2013) doi:10.1086/670067 [arXiv:1202.3665 [astro-ph.IM]].
- [67] L. Perivolaropoulos and F. Skara, *Universe* **8**, no.10, 502 (2022) doi:10.3390/universe8100502 [arXiv:2208.11169 [astro-ph.CO]].
- [68] H. Chaudhary, S. Capozziello, V. K. Sharma and G. Mustafa, *Astrophys. J.* **992**, no.2, 194 (2025) doi:10.3847/1538-4357/ae0458 [arXiv:2507.21607 [astro-ph.CO]].
- [69] E. Di Valentino, L. A. Anchordoqui, O. Akarsu, Y. Ali-Haimoud, L. Amendola, N. Arendse, M. Asgari, M. Ballardini, S. Basilakos and E. Battistelli, *et al.* *Astropart. Phys.* **131**, 102605 (2021) doi:10.1016/j.astropartphys.2021.102605 [arXiv:2008.11284 [astro-ph.CO]].

- [70] G. Efstathiou, Mon. Not. Roy. Astron. Soc. **505**, no.3, 3866-3872 (2021) doi:10.1093/mnras/stab1588 [arXiv:2103.08723 [astro-ph.CO]].
- [71] J. L. Bernal, L. Verde and A. G. Riess, JCAP **10**, 019 (2016) doi:10.1088/1475-7516/2016/10/019 [arXiv:1607.05617 [astro-ph.CO]].
- [72] M. Lopez-Hernandez, E. Ó. Colgáin, S. Pourojaghi and M. M. Sheikh-Jabbari, [arXiv:2510.04179 [astro-ph.CO]].
- [73] D. Camarena and V. Marra, Mon. Not. Roy. Astron. Soc. **504**, no.4, 5164-5171 (2021) doi:10.1093/mnras/stab1200 [arXiv:2101.08641 [astro-ph.CO]].
- [74] É. Aubourg *et al.* [BOSS], Phys. Rev. D **92**, no.12, 123516 (2015) doi:10.1103/PhysRevD.92.123516 [arXiv:1411.1074 [astro-ph.CO]].
- [75] E. Macaulay *et al.* [DES], Mon. Not. Roy. Astron. Soc. **486**, no.2, 2184-2196 (2019) doi:10.1093/mnras/stz978 [arXiv:1811.02376 [astro-ph.CO]].
- [76] A. Melchiorri, B. Paciello, P. Serra and A. Slosar, New J. Phys. **8**, 325 (2006) doi:10.1088/1367-2630/8/12/325
- [77] W. Yang, S. Pan, E. Di Valentino, O. Mena and A. Melchiorri, JCAP **10**, 008 (2021) doi:10.1088/1475-7516/2021/10/008 [arXiv:2101.03129 [astro-ph.CO]].